Resource competition predicts assembly of *in vitro* gut bacterial communities

Po-Yi Ho[1,*,#], Taylor H. Nguyen[1,*], Juan M. Sanchez[2], Brian C. DeFelice[2], Kerwyn Casey Huang[1,2,3,#]

[1]Department of Bioengineering, Stanford University, Stanford, CA, USA
[2]Chan Zuckerberg Biohub, San Francisco, CA 94158
[3]Department of Microbiology and Immunology, Stanford University School of Medicine, Stanford, CA 94305, USA

*: These authors contributed equally to this work.
#: Correspondence: poyiho@stanford.edu and kchuang@stanford.edu

ABSTRACT

Microbiota dynamics arise from a plethora of interspecies interactions[1-3], including resource competition[4-6], cross-feeding[7,8], and pH modulation[9,10]. The individual contributions of these mechanisms are challenging to untangle[11,12], especially in natural or complex laboratory environments where the landscape of resource competition is unclear. Here, we developed a framework to estimate the extent of multi-species niche overlaps by combining metabolomics data of individual species, growth measurements in pairwise spent media, and mathematical models. When applied to an *in vitro* model system of human gut commensals in complex media[13,14], our framework revealed that a simple model of resource competition described most pairwise interactions. By grouping metabolomic features depleted by the same set of species, we constructed a coarse-grained consumer-resource model that predicted assembly compositions to reasonable accuracy. Moreover, deviations from model predictions enabled us to identify and incorporate into the model additional interactions, including pH-mediated effects and cross-feeding, which improved model performance. In sum, our work provides an experimental and theoretical framework to dissect microbial interactions in complex *in vitro* environments.

INTRODUCTION

Microbial communities are important for host health and environmental functions[1,2], but their complex dynamics remain difficult to predict and engineer[3]. A major challenge is that community members affect each other through a plethora of interaction mechanisms, including resource competition[4-6], metabolic cross-feeding[7,8], pH modulation[9,10], toxins[15], and physical inhibition through secretion systems[16]. One approach to modeling the complexity of microbial interactions is to summarize the overall effects of species on each other using phenomenological interaction coefficients[11,17,18]. While phenomenological approaches can be predictive, they typically do not address the mechanistic origins of interactions, and thus are difficult to generalize[11,12,19]. A quantitative framework for microbiota dynamics based on species traits and interaction mechanisms is sorely needed[3,11,20].

To this end, consumer-resource (CR) models describe community dynamics under the basic mechanism of resource competition, which shapes community dynamics in diverse contexts ranging from simple synthetic communities to the human gut microbiota[21-24]. Notably, it was recently shown that a CR model could predict the dynamics of bottom-up assemblies of denitrifying bacteria[24]. This feat was achieved by measuring the denitrification rates of individual species in a chemically defined and electron-acceptor-limited growth medium, thereby quantifying resource competition in a minimal environment in which the limiting nutrients are known. However, it remains challenging to quantify resource competition in chemically undefined and complex nutrient environments such as the natural context of the gut microbiota[25-27].

Here, we sought to develop a trait-based modeling framework for microbiota dynamics in complex environments using stool-derived, *in vitro* communities that we previously established as an experimental model system for the gut microbiota of humanized mice, with similar compositions and responses to antibiotic treatment as observed *in vivo*[13,14]. We focused on 15 phylogenetically diverse species of human gut commensals isolated from the same parent *in vitro* community (**Fig. 1a**). We selected Brain Heart Infusion (BHI) as the growth medium because passaging of mouse fecal samples in BHI produced *in*

vitro communities that were most similar to their *in vivo* counterparts compared to other commonly used media[14]. When grown in BHI, these 15 species exhibited a broad range of growth phenotypes and assembled after 48 h into a community whose composition resembled that of the parent community[28] (**Extended Data Fig. 1**, **Supplementary Text**), indicating that this experimental setup may be informative of the *in vivo* context and is suitable for testing predictive models.

By assaying growth in media spent by the growth of other species, we show that a CR model can describe most pairwise species interactions. We then develop a novel approach that exploits the large number of unannotated metabolomic features in complex media to predict biomass yield in spent media, thereby enabling an estimation of the multi-species landscape of resource competition. Combining data from the metabolomics and spent-media experiments, we construct a CR model that predict assembly compositions to reasonable accuracy. Furthermore, we demonstrate a rational process to improve model predictions by identifying and incorporating additional interaction mechanisms, including cross-feeding and pH-mediated interactions. In sum, our findings establish a baseline model based on resource competition to predict community dynamics in complex nutrient environments, providing a framework to dissect microbial interactions and a step toward predictive models for natural microbiotas.

RESULTS

Most pairwise interactions can be described by a resource competition model

To characterize interspecies interactions in our model *in vitro* community (**Fig. 1a**), we measured the growth of each of the 15 species in isolation and in pairwise co-culture with each other species in BHI (**Methods**, **Fig. 1b**). In agreement with previous *in vitro* studies involving species from wide-ranging microbiotas[29], the 15 species typically inhibited the growth of one another in the sense that the null interaction score, the difference between the biomass yield (as measured by optical density) of the co-culture and the sum of the two individual yields, was negative in ≈89% of species pairs (93/105; **Fig. 1c**).

Since resource competition is a common form of interspecies inhibition, we sought to quantify its extent by measuring the growth of each species in the spent medium of each other species (**Methods**). Spent media exclude physical effects that would emerge due to the direct presence of a species, but maintain environmentally mediated interactions like resource competition. To interpret the results, we considered a CR model in which resources are completely consumed and converted to biomass by species growth[30,31]. We coarse-grained the model by grouping metabolites that are consumed by the same set of species into an effective resource. A community of two species is then described by three effective resources: two specifically consumed by one of the two species, and one shared by both species. Under this coarse-graining, species i grown individually will consume its specific resource and the shared resource, leaving the other resource specific to species j in the spent medium, while all three resources will be consumed in a co-culture of i and j (**Fig. 1b**). Hence, if all species convert resources into yield with the same efficiency, the model predicts a simple relation for the co-culture yield

$$\bar{X}_{i+j} = \bar{X}_i + \bar{X}_{j,i} = \bar{X}_j + \bar{X}_{i,j}, \quad (1)$$

where $\bar{X}_i$ is the yield of i in monoculture, $\bar{X}_{i,j}$ is the yield of i in the spent medium of j, and similarly for $\bar{X}_{j,i}$. Small values of resource competition residues $r(i,j) = \bar{X}_{i+j} - \left(\bar{X}_i + \bar{X}_{j,i}\right)$ and $r(j,i) = \bar{X}_{i+j} - \left(\bar{X}_j + \bar{X}_{i,j}\right)$ imply that Eq. 1 can describe the interactions between i and j, and hence, suggest that resource competition shapes this interaction. By contrast, large residues highlight deviations due to differences in metabolic efficiency or additional interactions. Note that the two residues $r(i,j)$ and $r(j,i)$ for a pair of species can be

asymmetric, potentially reflecting directionality of interactions as we demonstrate later. Although Eq. 1 makes several assumptions about resource utilization, it nonetheless provides a useful baseline to interpret interactions in spent media.

By contrast to the distribution of null interaction scores, the distribution of normalized resource competition residues $r(i,j)/\bar{X}_{i+j}$ and $r(j,i)/\bar{X}_{i+j}$ was centered about zero across the 210 ordered pairs (**Fig. 1d,e**). Simulations of random instances of the CR model used to derive Eq. 1 produced distributions of normalized residues centered about zero, as expected, and inclusion of empirical measurement noise for yield broadened the distribution to have a maximum magnitude of ≈0.2 (**Methods**, **Fig. 1d**). Almost 75% of all ordered pairs (155/210) had a residue with absolute value less than this maximum (**Fig. 1d,e**), indicating that their interactions were consistent with Eq. 1. If species utilize resources with different efficiencies, then these efficiencies can be determined from yields in monoculture and spent-media experiments similarly as in Eq. 1. The distribution of efficiencies was narrowly centered around one (**Extended Data Fig. 2a**), in agreement with Eq. 1 and its assumptions. Moreover, the model also predicts that the yield of species i in a 1:1 mixture of the individual spent medium of j and k should be equal to the average of the yields of i in each spent medium. This corollary was observed for the three-species combinations that we experimentally tested (**Fig. 1f**). Taken together, these results suggest that resource competition is an important driver of community dynamics in our system.

Metabolomic profiles capture the landscape of resource competition

To further interrogate resource competition, we obtained untargeted metabolomics data via liquid chromatography coupled with tandem mass spectrometry (LC-MS) on the spent medium of each species (**Methods**, **Fig. 2a**). Using an established pipeline designed to probe gut bacterial metabolism[32,33], we detected thousands of metabolomic peaks across ionization modes and chromatography methods ("features") in BHI, a chemically undefined medium. Although the vast majority of features could not be identified, the hundreds of features that were annotated included carbohydrates, nucleotides, and short peptides, collectively representing diverse metabolic pathways[33]. Therefore, we

hypothesized that the metabolomic profiles reflect the landscape of resource competition (i.e., the extent of resource sharing among species as well as the approximate sizes of individual and shared niches), and sought to predict species growth based on these data.

To connect metabolomic profiles and growth measurements, we would ideally be able to relate the signal intensity of a metabolite as reported by LC-MS to its contribution to biomass. However, one metabolite can generate multiple metabolomic features, the conversions from feature intensity to metabolite concentration can differ across metabolites, and conversions from metabolite concentration to biomass can differ across species[33,34]. In any case, these conversion factors are typically unknown. We reasoned that these details might be secondary to the total number of metabolites consumed in the limit of many involved metabolites, due to averaging over variations in these conversion factors. Accordingly, we tested the hypothesis that biomass yield is proportional to the number of features depleted (>100-fold depletion of signal intensity compared to fresh medium; **Methods**, **Fig. 2b**). This logic also predicts that the yield of species i in the spent medium of j should be proportional to the number of features depleted by i but not j. Since this hypothesis does not depend on metabolite identity, it enabled the incorporation of unannotated features. The resulting predictions were well correlated with experimental measurements of biomass yield (Pearson's correlation coefficient ρ = 0.78; **Fig. 2c**). Predictions using only the annotated metabolites were similarly well correlated (ρ = 0.54; **Extended Data Fig. 2b**). Analogous predictions for yields in co-cultures and in the spent media of co-cultures were also well correlated with these data and followed the same general trend as in the pairwise spent-media experiments (ρ = 0.65 and 0.74, respectively; **Fig. 2d,e**). Notably, successful predictions of the latter scenario indicate that multi-species interactions among the 3-species combinations tested were also captured. These results demonstrate that metabolomic profiles can approximate the resource competition landscape.

Resource competition approximately predicts community assembly

We next sought to use the metabolomics-based approximation of the resource competition landscape to predict the assembly of multiple species. We randomly selected

185 combinations of the 15 species while ensuring sampling among the various taxonomic families and community sizes, assembled them, and passaged their mixtures until they approximately reached an ecological steady state, defined as when subsequent passages exhibited identical dynamics. In practice, we found previously using similar *in vitro* communities that ecological steady state was approximately reached in five passages[14]. Finally, we obtained species relative abundances at ecological steady state by 16S rRNA gene sequencing (**Methods**). No assemblies were discarded during downstream analyses. We then constructed a coarse-grained CR model based on the monoculture metabolomics data and pairwise spent-media experiments, and tested to what extent it could predict assembly compositions (**Fig. 3a**).

Specifically, we considered the following model[31],

$$\frac{dX_i}{dt} = X_i \sum_{\mu=1}^{M} R_{i\mu} Y_\mu$$

$$\frac{dY_\mu}{dt} = -Y_\mu \sum_{i=1}^{N} R_{i\mu} X_i \,. \quad (2)$$

Here, X_i denotes the absolute abundance of species i, Y_μ the amount of coarse-grained resource μ, and $R_{i\mu}$ the consumption rate of resource μ by species i. Resources are assumed to be substitutable such that species growth continues until all resources are depleted. The efficiency of resource conversion into biomass is assumed to be the same for all species, and set to one such that resource amounts and species abundances are measured in the same unit. Key to this model is coarse-graining, the grouping of metabolites consumed by the same species into a coarse-grained resource ("resource group"). The same coarse-graining was used to derive Eq. 1, which is a special case of the dynamics explicitly described by Eq. 2. Coarse-graining ignores complexities in nutrient utilization such as hierarchical resource preferences, but enables an estimation of resource competition in complex nutrient environments.

To compare to experimental data, Eq. 2 was parametrized as described below and then simulated under serial dilution in which each dilution cycle continued until stationary

phase when all resources are depleted ($dY_\mu/dt = 0$), after which a new cycle was initiated by replenishing the resources to their initial levels Y_μ^0 and diluting all species abundances by a constant factor. Serial dilution was repeated until species abundances reached an ecological steady state in which further cycles produced virtually identical dynamics, mimicking the experimental protocol (**Methods**). For one species and one resource, this model described well the monoculture growth curves of the 15 species (**Methods**, **Extended Data Fig. 2c**). In a community context, species abundances at steady state $\bar{X}_i$ were independent of the initial abundances as long as the same species were initially present, consistent with previous studies involving similar formulations of CR models[31,35,36]. This independence was also observed experimentally for the following scenario: when dropout communities consisting of 14 of the 15 species were assembled and then mixed with the dropped-out species at ratios spanning five orders of magnitude, the resulting steady-state community compositions were virtually indistinguishable (**Methods**, **Extended Data Fig. 3**).

Since each coarse-grained resource group consists of many metabolites, the aggregate amount in fresh medium Y_μ^0 of group μ along with its associated consumption rates $R_{i\mu}$ are unknown. We decomposed the challenge of estimating these model parameters into three steps (**Methods**, **Fig. 3a**). The first step is to choose the set of resource groups that are incorporated into the model. Choosing this resource utilization structure is a core challenge because it is combinatorially complex. There are 2^{15} = 32,768 species combinations, and hence the same number of potential resource groups. Crucially, as we have seen, metabolomics data can directly reveal niche overlaps among multiple species (**Fig. 2**). The >15,000 features that were depleted in at least one spent medium grouped into ≈1,000 resource groups (**Extended Data Fig. 4a**). Most features fell into large groups, and the 100 groups with the most constituent features comprised 84% of all features. Notably, each species was associated with a set of features that it uniquely depleted, which collectively comprised 49% of all features (**Extended Data Fig. 4b**). Taking into account the above properties, we restricted our analysis to the 15 species-specific resource groups and the M groups with the most constituent features, reasoning

that these groups should encode most of the information about the resource competition landscape.

Given a set of resource groups, the second step is to estimate the $15+M$ unknown initial resource amounts Y_μ^0 via a linear regression in which the known variables are the experimentally determined yields in pairwise spent media (**Extended Data Fig. 5a**). Within the model, yield in spent media is equal to the sum of Y_μ^0 for μ consumed by the grown species but not the spent medium-generating species (**Methods**, **Fig. 3A**), analogous to the logic of Eq. 1. With this approach, the problem reduces to choosing the number M. To do so, we carried out the regression for each M, and chose the one that minimized the Akaike Information Criterion (AIC) of the regression for the final model (**Extended Data Fig. 5b**). Finally, consumption rates were inferred from the experimentally determined growth rates in spent media, following a similar logic as for resource levels (**Methods**).

The outcome was a set of resource levels and consumption rates for the 15 species (**Fig. 3a**). This CR model was numerically simulated to predict species abundances at ecological steady state for each of the 185 assemblies tested (**Extended Data Fig. 5c**). Model predictions were compared against experimental data using the absolute error of $\log_2$(fold-change) per species, defined as $\sum_{i=1}^{N}\left|\log_2\left(x_i^{\text{actual}}/x_i^{\text{predicted}}\right)\right|/N$, where $x_i = \bar{X}_i/\sum_{j=1}^{N}\bar{X}_j$ is the relative abundance at steady state of species i (which for this calculation was set to the detection threshold in our experiments, 10^{-4}, if i was undetectable; **Methods**). This error metric accounts for the compositional nature of relative abundance data by weighting errors in high- and low-abundance species equally in terms of fold-change[37], and can be interpreted intuitively as doublings per species.

Averaged across all assemblies tested, the mean error achieved by the model was 1.33 doublings per species (**Methods**, **Fig. 3b,c**, **Extended Data Fig. 5c-f**). Model error was only weakly correlated with the Shannon index (ρ = 0.18, p-value = 0.02; **Extended Data Fig. 5e**), demonstrating that model performance was robust to assembly diversity.

To evaluate the performance of this modeling approach, we tested several other approaches for parametrizing Eq. 2, briefly summarized below (**Methods**). First, we tested alternative methods to select the set of resource groups to include in the model, including three hypothetical resource utilization structures: 1) the base model consisting of the 15 species-specific groups, 2) the base model plus all pairwise niche overlaps, and 3) the base model plus all 15 all-but-one niche overlaps (**Extended Data Fig. 6a**). In addition, we tested resource utilization structures selected via regularized regression against all ≈1,000 resource groups detected by metabolomics (**Extended Data Fig. 6b**). We tested a different approach to parametrize the resource amount Y_μ^0 for the same resource utilization structure as before but based on metabolomic feature counts without regression against growth data in spent media. As an additional benchmark, we considered a null model in which the predictions of the CR model were shuffled with respect to species identity (**Extended Data Fig. 6c**). Finally, we examined several formulations of generalized Lotka-Volterra models with pairwise interspecies interactions (**Extended Data Fig. 6d,e**, **Supplementary Text**). Our CR model combining data from monoculture metabolomics and pairwise spent-media experiments predicted community assembly significantly better than all other approaches and models tested (Mann-Whitney U-test; **Fig. 3b**). This result was qualitatively robust when using the Bray-Curtis dissimilarity metric to assess error (**Extended Data Fig. 6f**), and model performance was similar when evaluated against estimates of absolute abundance obtained by multiplying experimentally determined relative abundance by culture yield (**Extended Data Fig. 6g**). Although these results do not rule out other models, they indicate that our CR model is a reasonable baseline for predicting community assembly.

The modeling framework above addressed several challenges posed by complex nutrient environments. First, the regressed resource levels Y_μ^0 recapitulated yields in spent media better than the number of metabolomic features alone (ρ = 0.91 versus 0.78; **Fig. 3d**), while remaining well correlated with feature counts excepting two groups with atypically large Y_μ^0 (ρ = 0.77 without these two outlier groups; **Extended Data Fig. 7a**). These groups contained features that were identified as the highly exploitable carbon sources glucose and trehalose, demonstrating that the incorporation of growth data fine-tuned the

metabolomics-based competition landscape in a manner consistent with biological expectations. Nonetheless, most incorporated groups did not contain any annotated features (**Extended Data Fig. 7b**), highlighting the ability of coarse-graining to harness information from the vast number of unannotated features. Second, coarse-graining circumvented some of the uncertainty in LC-MS measurements, as the large numbers involved made the resource utilization structure robust to noise in peak calling and quantification (**Extended Data Fig. 7c**).

To further test our CR model, we collected a time course of metabolomics data throughout a growth cycle of the full 15-species assembly and found that the model successfully predicted the dynamics of most coarse-grained resources (**Methods**, **Extended Data Fig. 8**). Additionally, errors in model predictions of resource dynamics were reduced through rational modification of the consumption rates, which simultaneously improved model predictions of species abundances (**Extended Data Fig. 8**). In sum, the above findings indicate that coarse-grained resource competition is a useful simplification of the complex dynamics in our system.

Rational incorporation of additional interaction mechanisms improves model predictions

While most pairs of species exhibited small resource competition residues, ≈25% of the residues deviated substantially from Eq. 1 (**Fig. 1d**). Deviations from Eq. 1 can arise in many ways. For example, if the growth of species i affects that of j by an amount Δ in addition to the assumptions of resource competition underlying Eq. 1 and this effect occurs similarly in spent medium and in co-culture, then the model would predict that $r(i,j) = \bar{X}_{i+j} - \left(\bar{X}_i + \bar{X}_{j,i}\right) = 0$ and $r(j,i) = \bar{X}_{i+j} - \left(\bar{X}_j + \bar{X}_{i,j}\right) = \Delta$ (**Fig. 4a**). If the effect of i on j is specific to spent medium and does not occur in co-culture, the model would instead predict $r(i,j) = -\Delta$ and $r(j,i) = 0$. A species involved in the latter scenario is *Blautia producta* (*Bp*), whose spent medium almost completely inhibited the growth of all other species, i.e., $\Delta < 0$ (**Fig. 4b**). However, *Bp* grew more slowly than many other species (**Extended Data Fig. 5a**), and thus, these other species were able to grow in co-culture before the inhibitory effects of *Bp* occurred. In agreement, the residues $r(Bp,j)$

were >0 for these other species *j* (**Fig. 4c**), indicating that there is a surplus of growth in co-culture relative to the inhibitory effects of *Bp*-spent medium.

We hypothesized that this inhibition could be mediated by pH. *Bp*-spent medium was highly acidic with pH ≈5, while the spent media of other species and the full community were mostly neutral (**Extended Data Fig. 9a**). Moreover, growth inhibition was largely lifted in *Bp*-spent medium that was adjusted to neutral pH (**Methods**, **Fig. 4b**). Residues computed from yields in pH-neutralized *Bp*-spent medium were less positive and closer to zero (**Fig. 4c**), demonstrating that pH neutralization brought these species pairs into closer agreement with Eq. 1 and its underlying CR model.

Within a model that accounts for only resource competition, growth inhibition can only be due to niche overlap. Therefore, the outsized inhibition by *Bp*-spent medium caused the regression to infer high levels for resources shared between *Bp* and other species but zero for the *Bp*-specific resource group (**Fig. 3a**). As a result, *Bp* was often predicted to go extinct, in disagreement with experimental data (**Fig. 3c**). Consequently, *Bp* was the species with the worst predictions (**Extended Data Fig. 5f**). By contrast, when the regression used yields from pH-neutralized *Bp*-spent medium, the *Bp*-specific resource group was inferred to have a non-zero level, which improved model predictions for *Bp* and overall (mean error = 1.31 doublings per species; **Fig. 4d**). These findings exemplify that while mechanisms other than resource competition can confound model parametrization, their effects can be disentangled and incorporated into the model in a rational manner.

Metabolic cross-feeding is another potential interaction mechanism. Of all metabolomic features in BHI that changed significantly in the spent medium of any of the species, <15% were produced (>10-fold increase in signal intensity relative to fresh medium) by at least one species. Of these produced features, <5% were consumed by at least one other species (**Fig. 2a**). The low percentages of produced and potentially cross-feeding metabolomic features detected suggest that cross-feeding interactions are uncommon in our system. Indeed, substantial growth promotion by spent media was rare. Only a single

ordered pair of species out of 210 exhibited strong enough growth promotion such that growth in spent medium surpassed that in fresh medium: the spent medium of *Escherichia fergusonii* (*Efe*) substantially boosted the growth of *Bacteroides thetaiotaomicron* (*Bt*), resulting in a positive residue, $r(Bt, Efe) > 0$ (**Fig. 4e**). This growth promotion persisted in larger assemblies (**Extended Data Fig. 9b-d**), and was likely due to the production of porphyrins, cofactors involved in iron metabolism that can stimulate the growth of certain Bacteroidetes[38].

To incorporate the beneficial effects of *Efe* on *Bt*, we modified the model by assuming that whenever *Efe* and *Bt* were both present, the predicted absolute abundance of *Bt* would be increased by a constant amount equal to the difference in yield between *Bt* grown in *Efe*-spent and fresh medium. Remarkably, without any additional tuning of model parameters, prediction errors decreased for all assemblies containing both *Efe* and *Bt* (**Fig. 4f**). By contrast, when the same modification was applied to *Bt* even when *Efe* was absent, prediction errors increased in some cases (**Fig. 4f**), implying that the enhanced growth of *Bt* was *Efe*-dependent. These findings demonstrate that cross-feeding interactions can also be incorporated into the model in a straightforward manner.

In addition to yield, lag time is another growth characteristic often affected by microbial interactions[39]. In our system, lag times in spent media and in the full community (estimated from the time course experiment) were correlated with, albeit somewhat longer than those in monoculture (**Extended Data Fig. 9e,f**). Incorporation of monoculture lag times into the model slightly improved predictions on average (mean error = 1.31 doublings per species; **Methods**), suggesting that a better understanding of lag times in community contexts could improve model predictions even further.

More generally, the above findings illustrate how deviations from model predictions can detect additional microbial interactions. When applied to another complex medium, mGAM, our approach revealed a set of interactions between several *Bacteroides* and Clostridia species that were not apparent in BHI (**Extended Data Fig. 10**, **Supplementary Text**), consistent with growing evidence that microbial interactions can

depend on the environment[3]. Nonetheless, the distribution of resource competition residues, the approximate proportionality between yield and feature count, and the overall performance of the CR model were qualitatively similar in mGAM as in BHI (**Extended Data Fig. 10**, **Supplementary Text**). Although an exhaustive investigation into the vast space of microbial interactions is outside the scope of this study, our results establish a rationally expandable and generalizable framework to dissect microbial ecology in complex environments.

DISCUSSION

Microbiome research is rapidly building toward high-throughput experimentation, and numerous experimental model systems with defined species compositions have recently been developed for natural microbiotas[40,41]. Motivated by the natural context, these systems typically use chemically undefined, complex media in which predictive, trait-based models are lacking. Here, we addressed this gap by developing a combined experimental and modeling framework. Rather than using relative abundance data to infer effective interspecies interactions, our framework builds a coarse-grained consumer-resource model for a system of N species using N monoculture metabolomics experiments and growth data in N^2 pairwise spent-media experiments. The resulting model can be applied to interrogate any of the 2^N possible species combinations. The model makes predictions by quantifying the resource competition landscape among all species, which also encodes higher-order resource competition among more than two species. For the *in vitro* gut bacterial communities investigated here, the model predicted assembly compositions to a mean error of $\approx$1.3 doublings per species.

Prediction error tended to be larger for assemblies with intermediate richness (**Extended Data Fig. 5e**), which can contain a relatively large number of species that interact by mechanisms other than resource competition due to random sampling, thereby increasing their prediction error. By contrast, assemblies with high richness will always be dominated by effective resource competition regardless of sampling since most species pairs have near-zero residues.

To obtain this level of accuracy, metabolomic feature counts were required to identify the set of resource groups to model. This coarse-graining process is a combinatorially complex problem and could be improved in future work. The resource level associated with each group must be refined using data from pairwise spent-media experiments. Although pairwise experiments are required, growth assays are more accessible and have higher throughput than sequencing of pairwise co-cultures, and can be feasibly applied to systems with hundreds of species. Building on this baseline model, cross-feeding and pH-mediated interactions could be incorporated to further improve

predictions. Future work should be able to build upon these findings to disentangle and quantify other interaction mechanisms, such as toxins and secretion systems.

Key to approximating the resource competition landscape was the proportionality between the number of metabolomic features and biomass yield. This surprising finding revealed that each of the 15 species had access to its own niche, which together comprised approximately half of all features and mechanistically explained the widespread coexistence of these species in various assemblies. Resources shared among multiple species comprised the remaining half of metabolomic features, as well as half of the total resource level in the model. Correspondingly, ignoring the shared resources led to $\approx 40\%$ more error in model predictions (**Fig. 3c**). Elucidating the conditions under which this proportionality holds may lead to better understanding of microbial interactions in complex nutrient environments. However, chemically undefined complex media cannot easily be separated into components, limiting direct tests of the effects of individual metabolites. For example, it remains unclear what constitutes the bulk of biomass precursors in BHI. Since peptone is an ingredient, a substantial fraction likely consists of short peptides, which shaped the resource competition landscape in our system (**Extended Data Fig. 7b**). The effects of vitamins, lipids, and other metabolite classes that we did not identify remain to be elucidated in future work.

Another limitation is that strain choice can potentially affect interactions, especially strongly negative interactions among mutually excluding strains that can result in complex behaviors such as multi-stability. Although systematic studies of this question are lacking, we found in another study that assembling type strains of the 15 species used here led to approximately the same community composition[42]. Moreover, robustness to variability in initial abundance was recently observed for the assembly in mice of >100 gut commensal strains from different donors[41], suggesting that such robustness is not exclusive to strains from the same microbiota nor to *in vitro* conditions.

Despite the above limitations, we envision that our framework can be applied to generate predictions for *in vitro* scenarios such as nutrient perturbation, resistance to invasion, and

community coalescence, which will facilitate understanding of their *in vivo* analogs of dietary change, pathogen infection, and fecal microbiota transplantation, respectively. For example, inulin simultaneously affects community composition and decreases burden from *C. difficile* infection in mouse models[43]. This decrease was linked to short chain fatty acids, metabolites associated with microbial metabolism of complex carbohydrates whose production by *Bacteroides* species has been implicated in colonization resistance against *Salmonella*[44]. Such interplay among diet, community composition, and colonization resistance can be further clarified by measuring resource competition landscapes in media supplemented with complex carbohydrates. In this way, the framework presented here provides a foundation for developing and deploying predictive models for natural microbiotas.

METHODS

Bacterial culturing

Isolates were obtained via plating of *in vitro* communities, derived from culturing fecal samples from humanized mice, on agar plates made with various complex media and frozen as glycerol stocks, as previously described[14,28]. Frozen stocks were streaked onto BHI-blood agar plates (5% defibrinated horse blood in 1.5% w/v agar). Resulting colonies were inoculated into 3 mL of Brain Heart Infusion (BHI) (BD #2237500) or modified Gifu Anaerobic Medium (mGAM) (HyServe #05433) in test tubes. All culturing was performed at 37 °C without shaking in an anaerobic chamber (Coy). To minimize potential physiological changes from freeze-thaw cycles and changes in growth medium, cultures were diluted 1:200 every 48 h for 3 passages before growth or metabolomics measurements. After the first passage, subsequent passages were performed in 96-well polystyrene plates (Greiner Bio-One #655161) filled with 200 µL of growth medium.

Bacterial growth measurements

Biomass yield over time was obtained via optical density at 600 nm (OD) as measured by an Epoch 2 plate reader (Biotek). All measurements were performed in clear, flat-bottomed 96-well plates (Greiner Bio-One #655161). Each well was filled with 200 µL of growth medium and inoculated with 1 µL of stationary phase culture immediately before measurement. Plates were sealed with transparent seals (Excel Scientific #STR-SEAL-PLT), with small ≈0.5 mm holes cut above each well to allow gas exchange. Holes were cut using a laser cutter with the sterile casing in place, minimizing contact that might result in contamination. Any contamination would be straightforwardly detected in assembly experiments involving known isolates, and we found no contamination for any such experiments in this study. Measurements were taken with continuous shaking at 37 °C.

Growth in spent media

Spent media were obtained by centrifuging saturated cultures at 4,000 × g for 5 min and filtering the supernatant with 0.22-µm polyethersulfone filters (Millex-GP #SLGP033RS) or 96-well 0.22-µm filter plates (Pall #8019). To investigate pH-mediated effects, *Bp*-spent medium was adjusted to a pH of 7.35 with NaOH, and filtered again to sterilize.

pH measurements via BCECF

pH measurements were obtained during plate reader measurements via the dual-excitation, ratiometric pH indicator 2',7-bis-(2-carboxyethyl)-5-(and-6)-carboxyfluorescein BCECF (Invitrogen #B1151). BCECF dissolved in DMSO (Fisher BioReagents #BP231) was diluted 1,000-fold into growth media to a final concentration of 1 mg/mL. Growth curves were obtained as described above, and in addition to absorbance, fluorescence was measured using monochromators at excitation/emission combinations 440 nm/535 nm and 490 nm/535 nm. pH values were obtained by calculating the ratio of the signals excited at 490 nm over 440 nm after subtracting background fluorescence, and calibrated to fresh medium set to various pH values.

Liquid chromatography-mass spectrometry (LC-MS/MS) metabolomics

Spent media were collected as described above and immediately stored at -80 °C. Samples were thawed only once, immediately before LC-MS/MS. Thawed samples were kept on ice, each sample was homogenized by pipetting prior to dispensing. Two 20-µL aliquots of supernatant were removed from each sample well and dispensed into two shallow 96-well polypropylene plates, maintained on ice. Additionally, 5 µL were removed from each sample and combined into a homogenous pool; this pool was dispensed in 20-µL aliquots and prepared in parallel with samples. These pooled samples were used for in-run quality control, injected at predefined intervals over the course of analysis to ensure consistent instrument performance over time. Samples were analyzed using two complementary chromatography methods: reversed phase (C18) and hydrophilic interaction chromatography (HILIC). All samples were analyzed by positive and negative mode electrospray ionization (ESI+, ESI-). Sample analysis order was randomized to minimize potential bias in data acquisition. Procedural blanks were prepared by extracting 20 µL of water in place of bacterial supernatant. Procedural blanks were inserted throughout the run as additional quality control.

HILIC analysis: Metabolites were extracted by adding 80 µL of extraction mixture containing a solution of acetonitrile and methanol (1:1), including 5% water and stabile

isotope-labeled internal standards, maintained at -20 °C. The extraction mixture was homogenized by pipetting, and the plate(s) was sealed and equilibrated in the -20 °C freezer for 1 h to ensure precipitation of any remaining protein. Plates were then placed in a centrifuge maintained at -9 °C and spun at 6,000 rcf for 5 min. Supernatant was removed and placed in a new 96-well plate for HILIC analysis. Internal standards were used to ensure complete injection of the sample and chromatographic integrity throughout the analysis. Two microliters of prepared sample were injected in each analysis.

Chromatographic separation parameters[32] and mass spectral parameters[33] were as described previously, with minor modifications. Briefly, spectra were collected using a Thermo Q Exactive HF Hybrid Quadrupole-Orbitrap mass spectrometer in both positive and negative mode ionization (separate injections, sequentially). Full MS-ddMS2 data was collected, an inclusion list was used to prioritize MS2 selection of metabolites from an in-house library. Additional scan bandwidth allowed for MS2 collection in a data-dependent manner. Mass range was 60-900 *m*/*z*, resolution was 60k (MS1) and 15k (MS2), centroid data was collected, loop count was 4, and the isolation window was 1.2 Da.

C18 analysis: Metabolites for C18 analysis were prepared similarly to HILIC analysis, with slight modification. Briefly, the extraction solution for C18 analysis was -20 °C MeOH containing internal standards. Subsequent steps matched the HILC procedure described above. In addition to the HILIC protocol, C18-analyzed samples were dried using a Labconco Centrivap at room temperature. Once dried, samples were stored at -20 °C until analysis, when analyzed samples were reconstituted in 20% acetonitrile in water and placed in the autosampler maintained at 4 °C.

Two microliters of prepared sample were injected onto an Agilent SB-C18 column (100 mm length × 3.0 mm inner diameter; 1.8-µm particle size) with a Phenomenex KrudKatcher Ultra filter frit attached to the column inlet. The column was maintained at 40 °C coupled to an Thermo Vanquish UPLC. The mobile phases were prepared with 0.1% formic acid in LC-MS grade water for mobile phase A or 100% LC-MS grade

acetonitrile for mobile phase B. Gradient elution was performed from 3% (B) at 0–0.43 min to 97% (B) at 9 min, isocratic until 11 min, returning to 3% (B) at 11.5 min and maintained isocratically until 14 min. Column flow was maintained at 0.4 mL/min. Spectra were collected using a Thermo Q Exactive HF Hybrid Quadrupole-Orbitrap mass spectrometer in both positive and negative mode ionization (separate injections). Full MS-ddMS2 data were collected, an inclusion list was used to prioritize MS2 selection of metabolites from an in-house library. Additional scan bandwidth allowed for MS2 collection in a data-dependent manner. Mass range was 60-900 *m*/*z*, resolution was 60k (MS1) and 15k (MS2), centroid data was collected, loop count was 4, and the isolation window was 1.0 Da.

Data was processed using MS-DIAL v. 4.60[45,46]. MS1 tolerance was set to 0.01 Da, MS2 tolerance set to 0.015 Da, and minimum peak height was set to 100k. Alignment retention time tolerance was set to 0.05 min, and mass tolerance was set to 0.015 Da. Annotations were based on in-house libraries of standards analyzed using these chromatographic methods. The freely available MassBank of North America MS2 repository (https://mona.fiehnlab.ucdavis.edu/) was used for annotations of metabolites not found in our library. All annotations were MS2-based. Aligned peaks were retained for further analyses only if they were present in at least two of three replicates and were >5-fold higher than the water blank average in at least one sample.

Assembly experiments

Communities were assembled from stationary phase cultures of isolates mixed at equal volume, and 1 µL of the mixture was inoculated into 200 µL of growth medium. Plates were sealed and incubated at 37 °C without shaking. The assemblies were diluted 1:200 into fresh medium every 48 h for 5 passages to approximately reach an ecological steady state, defined as when subsequent passages exhibited identical dynamics. Using *in vitro* communities similar to the ones in this study, we previously found that ecological steady state was reached in approximately five passages[14]. The 15 single-species “dropout” assemblies with 14 of the 15 members were serially diluted for only 3 passages. In “refill” experiments, the inoculum for each dropout was mixed 1:1, 1:10, 1:100, 1:1,000, or

1:10,000 with a monoculture of the species that was left out and passaged 3 times. The final passage for assembly experiments was grown in a plate reader for OD measurements, after which the plate was stored at -80 °C until DNA extraction for 16S rRNA gene sequencing was performed.

Time course experiment

The full community of 15 species was assembled and passaged via serial dilution until ecological steady state. Using one culture of the full community in stationary phase, 72 replicate cultures were inoculated into fresh media. At each of 24 time points throughout the next growth cycle (at 1, 2, 3, 4, 5, 6, 7, 8, 9, 10, 11, 12, 14, 16, 18, 20, 22, 24, 28, 32, 36, 40, 44, and 48 h), 3 replicate samples were collected. Cells were pelleted by centrifuging at $4{,}000 \times g$ for 5 min, separated from supernatants, and stored for sequencing. Supernatants were stored for metabolomics. The result was a time course of sequencing and metabolomics data representing the dynamics of the full community.

Summary of experiments

Several sets of experiments involved combinations of species, which are summarized here for clarity. The following growth measurements were carried out: 1) all monoculture, pairwise spent-media, and pairwise co-culture experiments; 2) a subset of 3-species combinations for which a species was grown in the mixture of the individual spent media of two other species; 3) a subset of 3-species combinations for which a species was grown in the spent medium of the co-culture of two other species. For the 3-species combinations, the species used for growth measurements were chosen based on exhibiting high yield in monoculture to ensure a broad range of growth behaviors, and the other two species were randomly selected; these combinations are listed in the corresponding figure legends. In addition, 185 combinations of a subset of the 15 species, randomly selected while ensuring sampling across community sizes and taxonomic families, were assembled as described above. The full list of assemblies is shown in **Extended Data Fig. 5c,d**.

16S rRNA gene sequencing and analyses

Amplicon sequencing data were obtained and processed as previously described[14,47]: DNA was extracted from 50 mL of culture using the DNeasy UltraClean 96 Microbial Kit (Qiagen #10196-4). The bacterial 16S rRNA V4 region was amplified with Earth Microbiome Project-recommended 515F/806R primer pairs using the 5PRIME HotMasterMix (Quantabio #2200410) with the following thermocycler program: 94 °C for 3 min, 35 cycles of [94 °C for 45 s, 50 °C for 60 s, and 72 °C for 90 s], followed by 72 °C for 10 min. PCR products were cleaned with the UltraClean 96 PCR Cleanup kit (Qiagen #12596-4) and pooled using the same volume for each sample. Pooled libraries were concentrated by ethanol precipitation and purified by gel extraction of the corresponding library size using the NucleoSpin Gel and PCR Clean-up Mini kit (Macherey-Nagel). Libraries were prepared using the MiSeq Reagent Kit v3 with 300-bp paired-end reads and sequenced on a MiSeq (Illumina). Demultiplexed fastq files for each sample were processed using DADA2 (*46*) with the following parameters for the "filterAndTrim" function: [truncLenF = 240, truncLenR = 160, maxEE = c(2,2), truncQ = 2, maxN = 0]. Default parameters were used for the "learnErrors" and "dada" functions. Taxonomic assignment was performed with the "assignTaxonomy" function using the Greengenes Database (gg_13_8_train_set_97.fa).

Relative abundances were determined to a minimum threshold of 10^{-4}, reflecting the typical depth of sequencing, and the relative abundance of undetected species was set to 10^{-4} for visualization and for calculating the error between model predictions and experimental data. The three *Enterococcus* species were indistinguishable by the amplicon protocol used here. When more than one was present, their relative abundances were summed and visualized as *Eh* if *Eh* was present, else as *Efs*.

Analyses of growth curves

OD measurements were calibrated to be proportional to cell density by linear interpolation to data obtained in a previous study[48]. The minimum point of each growth curve was subtracted as a proxy for the background absorbance. To extract the final yield $\bar{X}$ and growth rate λ, each growth curve was fit to Eq. 2, modified to incorporate a lag time τ, with one species and one resource. Prior to the time τ, the species does not consume

resources nor grow, which was implemented by multiplying X by the step function $\theta(t-\tau)$, where $\theta(t)$ = 1 for $t \geq 0$ and 0 otherwise. The culture yield over time $X(t)$ becomes

$$X(t) = \bar{X}\left[1 + (\bar{X}/X_0 - 1)\exp\left(-\lambda(t-\tau)\right)\right]^{-1},$$

where $\lambda = RY(t=0)$ is the growth rate, $X_0 = X(t=0)$ is the initial abundance, and $\bar{X} = X(t = 48\text{ h})$ is the yield at 48 h (defined as such to match our experimental protocol). The growth rate λ and lag time τ were determined by exhaustive grid search minimizing the mean squared error between predicted and measured $X(t)$. Unless otherwise stated, lag time was not included in simulations of community dynamics.

Analyses of metabolomics data

Metabolomic features that passed pre-processing were defined as depleted or produced if they decreased by >100-fold or increased by >10-fold, respectively, compared to fresh medium, and if the difference was significant (p<0.05) by a two-sample t-test. An ion intensity of 0 was set to 1 for the purpose of calculating fold changes. Coarse-grained resource groups were obtained by grouping metabolomic features that shared the same set of depleting species.

Residues in randomly generated coarse-grained CR models

To determine the typical distribution of resource competition residues in coarse-grained CR models, 100 resource groups were randomly selected out of all possible groupings of 15 species. Each group was assigned a random initial level from a uniform distribution from 0 to 1. Simulated yields of monoculture and pairwise spent-media experiments were then calculated directly by summing the levels of the consumed resource groups. The resulting yields were modified with empirical measurement noise before calculating the resource competition residues.

Simulations of the coarse-grained CR model

To mimic our experimental protocol, Eq. 2 was simulated under a serial dilution scheme in which each dilution cycle continued until stationary phase when all resources are depleted ($dY_\mu/dt = 0$ for all μ), after which a new cycle was initiated by replenishing the

resources to their initial levels Y_μ^0 and diluting all species abundances by a factor D, which was set to 200 in simulations to mimic our experimental protocol. In simulations, the first cycle was initialized with equal abundances of each species, and dilutions were repeated until an ecological steady state was reached in which further cycles produced identical dynamics up to a small numerical threshold. At ecological steady state, species abundances in stationary phase are linear combinations of the resource levels since all resources have been converted to biomass, and are independent of the initial abundances given the same set of initially present species[31,35,36]. Note that X_i in Eq. 2 denotes absolute abundances, and all simulations were carried out using absolute abundances. To compare against experimental data, simulation results were converted to relative abundances and those $<10^{-4}$ were considered undetectable and removed in downstream calculations.

Parametrization of the coarse-grained CR model

The parameters of the CR model in Eq. 2 are the resource levels in fresh medium Y_μ^0 and resource consumption rates $R_{i\mu}$, which were inferred as briefly described in the text. In greater detail, given a resource utilization structure defined by a set of coarse-grained resource groups, the corresponding resource levels were inferred from the experimentally determined yield $\bar{X}_{i,j}$ of species i in the spent medium of j, which the model predicts to be $\bar{X}_{i,j} = \sum_{\mu \in S_i \setminus S_j} Y_\mu^0$. Here, S_i is the set of resources consumed by species i, and "\" denotes the difference between sets. In other words, the sum is over resources μ consumed by i but not j such that $R_{i\mu} > 0$ but $R_{j\mu} = 0$. Since the resource utilization structure is given, which elements of $R_{i\mu}$ are non-zero is known (although their values are not yet known). Each of the 15^2 experiments in monoculture and pairwise spent media represented one equation in the non-negative least squares regression. The M resource groups with the most constituent features to incorporate into the model was determined by minimizing the AIC assuming that residuals from the regression are normally distributed with zero mean and variance equal to the observed sample variance. This minimization was carried out to a maximum of 50 groups to avoid overfitting (**Extended Data Fig. 5b**). Including more groups did not improve model predictions. Resources μ

inferred to have near-zero Y_μ^0 (<10^{-4}) were removed from the model. The consumption rates $R_{i\mu}$ were similarly inferred from the experimentally determined growth rates, which the model predicts to have a maximum value of $\lambda_{i,j}^{\max} = \sum_{\mu \in S_i \setminus S_j} R_{i\mu} Y_\mu^0$ for species i grown in the spent medium of species j. Given limitations in the accuracy of growth rate measurements in cultures with low yield, we further simplified the problem and assumed that $R_{i\mu} = R_i^*$ for all resources μ, i.e., species i consumes all resources that it uses at the same rate, and hence, $R_i^* = \lambda_i / \sum_{\mu \in S_i} Y_\mu^0$.

Comparison with hypothetical resource utilization structures

To evaluate the relevance of metabolomics-derived resource groups, three hypothetical structures of resource consumption were used to predict assembly compositions: a "base" structure that included only the 15 species-specific groups, and on top of this base structure, either every group shared between species pairs, or every group shared across all but one species (**Extended Data Fig. 4a**). For each of these structures, a set of resource levels and consumption rates was inferred from pairwise spent-media experiments following the procedure described above.

Comparison with resource utilization structures selected via regularized regression

In addition to using resource groups with the most constituent features to determine the resource utilization structure, we tested another approach via LASSO. The LASSO analysis used all detected resource groups to construct the regression problem from pairwise spent-media experiments. Hence, for the same 15^2 known variables as in the original regression problem, there were as many unknowns as the number of detected groups, ≈1,000. A regularization parameter penalized against having many resources with non-zero values of Y_μ^0. The regularization parameter was varied across a broad range, which resulted in a minimum of 1 and a maximum of 45 resources with non-zero Y_μ^0. Each value of the regularization parameter led to a set of inferred resource levels and consumption rates (**Extended Data Fig. 6b**). LASSO performance was defined as the mean error of the best-performing set (**Fig. 3b**).

Comparison with model based on the number of metabolomic features alone

To estimate resource levels Y_μ^0, one option is to set Y_μ^0 proportional to the number of metabolomic features in resource group μ, without fine-tuning via regression against yields in spent media. To test the performance of this parametrization, the resource utilization structure was kept the same as in **Fig. 3a**, the proportionality constant between feature count and resource level Y_μ^0 was set to the best fit value from the pairwise spent-media experiments (**Fig. 2c**), and resource consumption rates were determined in the manner described above.

REFERENCES

1 Cho, I. & Blaser, M. J. The human microbiome: at the interface of health and disease. *Nature Reviews Genetics* **13**, 260-270 (2012). https://doi.org:10.1038/nrg3182

2 Singh, B. K., Trivedi, P., Egidi, E., MacDonald, C. A. & Delgado-Baquerizo, M. Crop microbiome and sustainable agriculture. *Nature Reviews Microbiology* **18**, 601-602 (2020). https://doi.org:10.1038/s41579-020-00446-y

3 Widder, S. *et al.* Challenges in microbial ecology: building predictive understanding of community function and dynamics. *The ISME Journal* **10**, 2557-2568 (2016). https://doi.org:10.1038/ismej.2016.45

4 Niehaus, L. *et al.* Microbial coexistence through chemical-mediated interactions. *Nature Communications* **10**, 2052 (2019). https://doi.org:10.1038/s41467-019-10062-x

5 Hammarlund, S. P., Gedeon, T., Carlson, R. P. & Harcombe, W. R. Limitation by a shared mutualist promotes coexistence of multiple competing partners. *Nature Communications* **12**, 619 (2021). https://doi.org:10.1038/s41467-021-20922-0

6 Dal Bello, M., Lee, H., Goyal, A. & Gore, J. Resource–diversity relationships in bacterial communities reflect the network structure of microbial metabolism. *Nature Ecology & Evolution* **5**, 1424-1434 (2021). https://doi.org:10.1038/s41559-021-01535-8

7 Adamowicz, E. M., Flynn, J., Hunter, R. C. & Harcombe, W. R. Cross-feeding modulates antibiotic tolerance in bacterial communities. *The ISME Journal* **12**, 2723-2735 (2018). https://doi.org:10.1038/s41396-018-0212-z

8 Amarnath, K. *et al.* Stress-induced cross-feeding of internal metabolites provides a dynamic mechanism of microbial cooperation. *bioRxiv*, 2021.2006.2024.449802 (2021). https://doi.org:10.1101/2021.06.24.449802

9 Ratzke, C. & Gore, J. Modifying and reacting to the environmental pH can drive bacterial interactions. *PLoS biology* **16**, e2004248 (2018).

10 Aranda-Díaz, A. *et al.* Bacterial interspecies interactions modulate pH-mediated antibiotic tolerance. *eLife* **9**, e51493 (2020).

11 Faust, K. & Raes, J. Microbial interactions: from networks to models. *Nature Reviews Microbiology* **10**, 538-550 (2012). https://doi.org:10.1038/nrmicro2832

12 Momeni, B., Xie, L. & Shou, W. Lotka-Volterra pairwise modeling fails to capture diverse pairwise microbial interactions. *eLife* **6**, e25051 (2017).

13 Ng, K. M. *et al.* Recovery of the gut microbiota after antibiotics depends on host diet, community context, and environmental reservoirs. *Cell host & microbe* **26**, 650-665 (2019).

14 Aranda-Díaz, A. *et al.* Establishment and characterization of stable, diverse, fecal-derived in vitro microbial communities that model the intestinal microbiota. *Cell Host & Microbe* (2022). https://doi.org:https://doi.org/10.1016/j.chom.2021.12.008

15 Wexler, A. G. *et al.* Human symbionts inject and neutralize antibacterial toxins to persist in the gut. *Proceedings of the National Academy of Sciences* **113**, 3639-3644 (2016). https://doi.org:10.1073/pnas.1525637113

16 Verster, A. J. *et al.* The Landscape of Type VI Secretion across Human Gut Microbiomes Reveals Its Role in Community Composition. *Cell Host & Microbe* **22**, 411-419.e414 (2017). https://doi.org:10.1016/j.chom.2017.08.010

17 Venturelli, O. S. *et al.* Deciphering microbial interactions in synthetic human gut microbiome communities. *Molecular Systems Biology* **14**, e8157 (2018). https://doi.org:https://doi.org/10.15252/msb.20178157

18 Hu, J., Amor, D. R., Barbier, M., Bunin, G. & Gore, J. Emergent phases of ecological diversity and dynamics mapped in microcosms. *Science* **378**, 85-89 (2022). https://doi.org:10.1126/science.abm7841

19 Fisher, C. K. & Mehta, P. Identifying Keystone Species in the Human Gut Microbiome from Metagenomic Timeseries Using Sparse Linear Regression. *PLOS ONE* **9**, e102451 (2014).

20 Martiny, J. B. H., Jones, S. E., Lennon, J. T. & Martiny, A. C. Microbiomes in light of traits: A phylogenetic perspective. *Science* **350**, aac9323 (2015). https://doi.org:10.1126/science.aac9323

21 Chesson, P. MacArthur's consumer-resource model. *Theoretical Population Biology* **37**, 26-38 (1990).

22 Hart, S. F. M. *et al.* Uncovering and resolving challenges of quantitative modeling in a simplified community of interacting cells. *PLOS Biology* **17**, e3000135 (2019).

23 Patnode, M. L. *et al.* Interspecies Competition Impacts Targeted Manipulation of Human Gut Bacteria by Fiber-Derived Glycans. *Cell* **179**, 59-73.e13 (2019). https://doi.org:10.1016/j.cell.2019.08.011

24 Gowda, K., Ping, D., Mani, M. & Kuehn, S. Genomic structure predicts metabolite dynamics in microbial communities. *Cell* **185**, 530-546.e525 (2022). https://doi.org:https://doi.org/10.1016/j.cell.2021.12.036

25 Biggs, M. B. *et al.* Systems-level metabolism of the altered Schaedler flora, a complete gut microbiota. *The ISME Journal* **11**, 426-438 (2017). https://doi.org:10.1038/ismej.2016.130

26 Medlock, G. L. *et al.* Inferring Metabolic Mechanisms of Interaction within a Defined Gut Microbiota. *Cell Systems* **7**, 245-257.e247 (2018). https://doi.org:https://doi.org/10.1016/j.cels.2018.08.003

27 Weiss, A. S. *et al.* In vitro interaction network of a synthetic gut bacterial community. *The ISME Journal* (2021). https://doi.org:10.1038/s41396-021-01153-z

28 Aranda-Diaz, A. *et al.* Assembly of gut-derived bacterial communities follows" early-bird" resource utilization dynamics. *bioRxiv*, 2023.2001. 2013.523996 (2023).

29 Foster, Kevin R. & Bell, T. Competition, Not Cooperation, Dominates Interactions among Culturable Microbial Species. *Current Biology* **22**, 1845-1850 (2012). https://doi.org:https://doi.org/10.1016/j.cub.2012.08.005

30 Erez, A., Lopez, J. G., Weiner, B. G., Meir, Y. & Wingreen, N. S. Nutrient levels and trade-offs control diversity in a serial dilution ecosystem. *Elife* **9**, e57790 (2020).

31 Ho, P.-Y., Good, B. H. & Huang, K. C. Competition for fluctuating resources reproduces statistics of species abundance over time across wide-ranging microbiotas. *eLife* **11**, e75168

32 Showalter, M. R. *et al.* Obesogenic diets alter metabolism in mice. *PLOS ONE* **13**, e0190632 (2018).

33 Han, S. *et al.* A metabolomics pipeline for the mechanistic interrogation of the gut microbiome. *Nature* **595**, 415-420 (2021). https://doi.org:10.1038/s41586-021-03707-9

34 Alseekh, S. *et al.* Mass spectrometry-based metabolomics: a guide for annotation, quantification and best reporting practices. *Nature Methods* **18**, 747-756 (2021). https://doi.org:10.1038/s41592-021-01197-1

35 Xiao, Y. *et al.* Mapping the ecological networks of microbial communities. *Nature Communications* **8**, 2042 (2017). https://doi.org:10.1038/s41467-017-02090-2

36 Cui, W., Marsland, R. & Mehta, P. Diverse communities behave like typical random ecosystems. *Physical Review E* **104**, 034416 (2021). https://doi.org:10.1103/PhysRevE.104.034416

37 Gloor, G. B., Macklaim, J. M., Pawlowsky-Glahn, V. & Egozcue, J. J. Microbiome Datasets Are Compositional: And This Is Not Optional. *Frontiers in Microbiology* **8** (2017).

38 Halpern, D. & Gruss, A. A sensitive bacterial-growth-based test reveals how intestinal Bacteroides meet their porphyrin requirement. *BMC Microbiology* **15**, 282 (2015). https://doi.org:10.1186/s12866-015-0616-0

39 Bloxham, B., Lee, H. & Gore, J. Diauxic lags explain unexpected coexistence in multi-resource environments. *Molecular Systems Biology* **18**, e10630 (2022). https://doi.org:https://doi.org/10.15252/msb.202110630

40 Bai, Y. *et al.* Functional overlap of the Arabidopsis leaf and root microbiota. *Nature* **528**, 364-369 (2015). https://doi.org:10.1038/nature16192

41 Cheng, A. G. *et al.* Design, construction, and in vivo augmentation of a complex gut microbiome. *Cell* **185**, 3617-3636.e3619 (2022). https://doi.org:https://doi.org/10.1016/j.cell.2022.08.003

42 Aranda-Díaz, A. *et al.* High-throughput cultivation of stable, diverse, fecal-derived microbial communities to model the intestinal microbiota. *BioRxiv*, 2020.2007.2006.190181 (2020).

43 Hryckowian, A. J. *et al.* Microbiota-accessible carbohydrates suppress Clostridium difficile infection in a murine model. *Nature Microbiology* **3**, 662-669 (2018). https://doi.org:10.1038/s41564-018-0150-6

44 Jacobson, A. *et al.* A Gut Commensal-Produced Metabolite Mediates Colonization Resistance to Salmonella Infection. *Cell Host & Microbe* **24**, 296-307.e297 (2018). https://doi.org:https://doi.org/10.1016/j.chom.2018.07.002

45 Tsugawa, H. *et al.* MS-DIAL: data-independent MS/MS deconvolution for comprehensive metabolome analysis. *Nature Methods* **12**, 523-526 (2015). https://doi.org:10.1038/nmeth.3393

46 Tsugawa, H. *et al.* A lipidome atlas in MS-DIAL 4. *Nature Biotechnology* **38**, 1159-1163 (2020). https://doi.org:10.1038/s41587-020-0531-2

47 Celis, A. I. *et al. iScience* **25** (2022). https://doi.org:10.1016/j.isci.2022.103907

48 Atolia, E. *et al.* Environmental and Physiological Factors Affecting High-Throughput Measurements of Bacterial Growth. *mBio* **11**, e01378-01320 (2020). https://doi.org:10.1128/mBio.01378-20

ACKNOWLEDGMENTS

We thank members of the Huang lab for helpful discussions, and Jonas Cremer, Ben Good, Karna Gowda, Mikhail Tikhonov, Ned Wingreen, and Katherine Xue for critical readings of the manuscript. We thank Biohub team member Wasim Sandhu for metabolite extraction and LC-MS/MS data acquisition. This work was funded by a Stanford School of Medicine Dean's Postdoctoral Fellowship (to P.H.), an NIH Postdoctoral Fellowship F32 GM143859 (to P.H.), an NSF Graduate Research Fellowship (to T.H.N.), NSF Awards EF-2125383 and IOS-2032985 (to K.C.H.), and NIH Awards R01 AI147023 and RM1 GM135102 (to K.C.H.). K.C.H. is a Chan Zuckerberg Biohub Investigator.

Author contributions: Conceptualization: PH, KCH. Methodology: PH, THN, BCD, KCH. Investigation: PH, THN, JMS, BCD. Visualization: PH, THN, KCH. Funding acquisition: PH, THN, KCH. Supervision: PH, BCD, KCH. Writing – original draft: PH, THN, KCH. Writing – review & editing: PH, THN, BCD, KCH.

Competing interests: The authors declare that they have no competing interests.

Data availability: All data are available at the Zenodo repository (10.5281/zenodo.7535703). Metabolomics data are available in the NIH Metabolomics Workbench under ST002832, ST002833, and ST002834. Sequencing data are available under ENA study PRJEB72096.

Code availability: All code are available at the Zenodo repository (10.5281/zenodo.7535703).

Supplementary Information: Supplementary Text

FIGURES

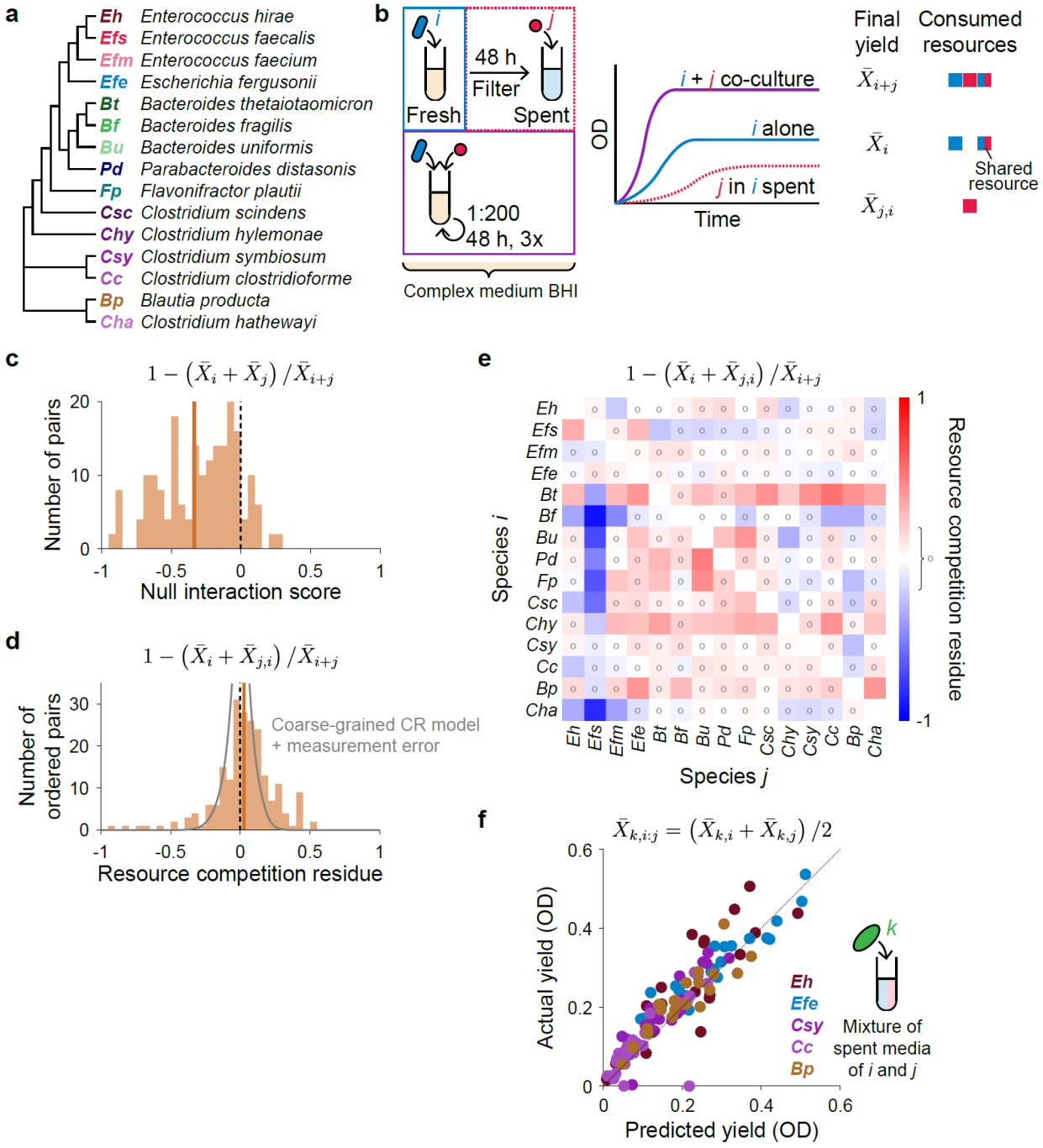

Figure 1: Coarse-grained resource competition can describe most pairwise interactions in an *in vitro* model system of 15 human gut commensals.

a) Phylogenetic tree of the 15 species studied here, which collectively represent an experimental model system for the gut microbiota of humanized mice[14] (**Extended Data Fig. 1**, **Supplementary Text**).

b) Schematic of growth experiments in pairwise spent media and predictions of the coarse-grained CR model. Growth curves of optical density (OD) over time were obtained for each species grown in monoculture, in co-culture with every other species, and in the spent media of every other species, all in the complex medium BHI (**Methods**). In the coarse-grained CR model, the final yield is determined by the amount of coarse-grained resources, resulting in Eq. 1.

c) The null interaction score, the difference between the yield $\bar{X}_{i+j}$ of the co-culture of species i and j and the sum of the individual yields $\bar{X}_i$ and $\bar{X}_j$, was negative for most species pairs. Shown in (c-f) are mean yields across replicates. Solid vertical line denotes the mean across all pairs.

d) The distribution of normalized resource competition residues was centered about zero. Shown in gray are results for numerical simulations of randomly generated coarse-grained CR models with empirical error in yield measurements (**Methods**).

e) Most normalized resource competition residues were close to zero. Circles “o” denote residues with absolute value <0.2, the approximate maximum value of residues in simulations of randomly generated coarse-grained CR models in (d).

f) Yield in 1:1 mixtures of spent media was predicted by the average of the yield in each spent medium individually. For feasibility, only a subset of all 3-species combinations was tested. Five species, denoted by colors, were grown in every pairwise mixture of the spent media from *Eh*, *Efe*, *Csy*, *Bt*, *Bp*, *Csc*, *Efs* or fresh BHI (**Methods**).

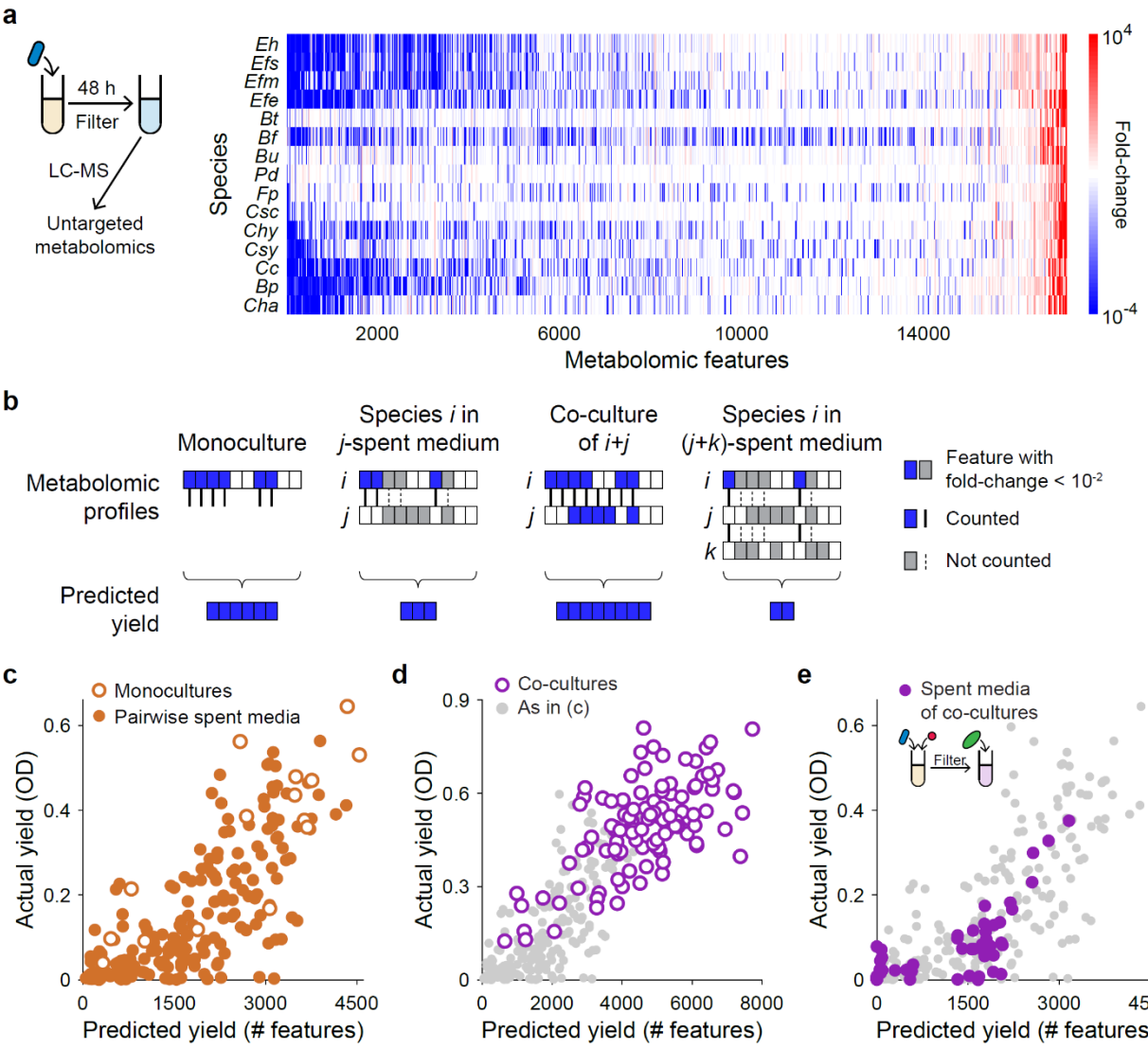

Figure 2: Metabolomic profiles can approximately predict yield in monoculture, co-culture, and spent media.

a) Schematic of metabolomics experiments and the resulting profile of fold change in LC-MS signal intensity relative to fresh BHI for each species. Shown are mean values across three replicates for all metabolomic features, including unannotated ones, that changed significantly in the spent medium of any of the species (**Methods**).

b) Schematic of rule used to predict yield from metabolomic profiles. The predicted yield of a species in monoculture was defined as the number of metabolomic features (rectangles) that was depleted in the spent medium of that species (blue, solid lines). The predicted yield of species i in the spent medium of j was defined

as the number of features depleted by i but not j (gray, dashed lines), and analogously for co-cultures of i and j, as well as i growing in the co-culture of j and k.

c) Feature count was correlated with biomass yield in monocultures and pairwise spent-media experiments (Pearson's correlation coefficient ρ = 0.83, 0.76, and 0.78 for monocultures, pairwise spent-media experiments, and together, respectively). Shown in (c-e) are mean yields across replicates.

d) The same trend was also observed for pairwise co-cultures (ρ = 0.65). All pairwise co-cultures are shown. Monocultures and pairwise spent-media experiments, as in (c), are shown in gray in (d,e) as a visual guide.

e) The same trend was also observed for yield in the spent medium of co-cultures (ρ = 0.74). For feasibility, only a subset of all 3-species combinations was tested. Two species (*Eh* and *Efe*) were grown in the spent media of all pairwise co-cultures of *Eh*, *Efe*, *Csy*, *Bt*, *Cc*, *Bp*, *Csc*, and *Efs* (**Methods**).

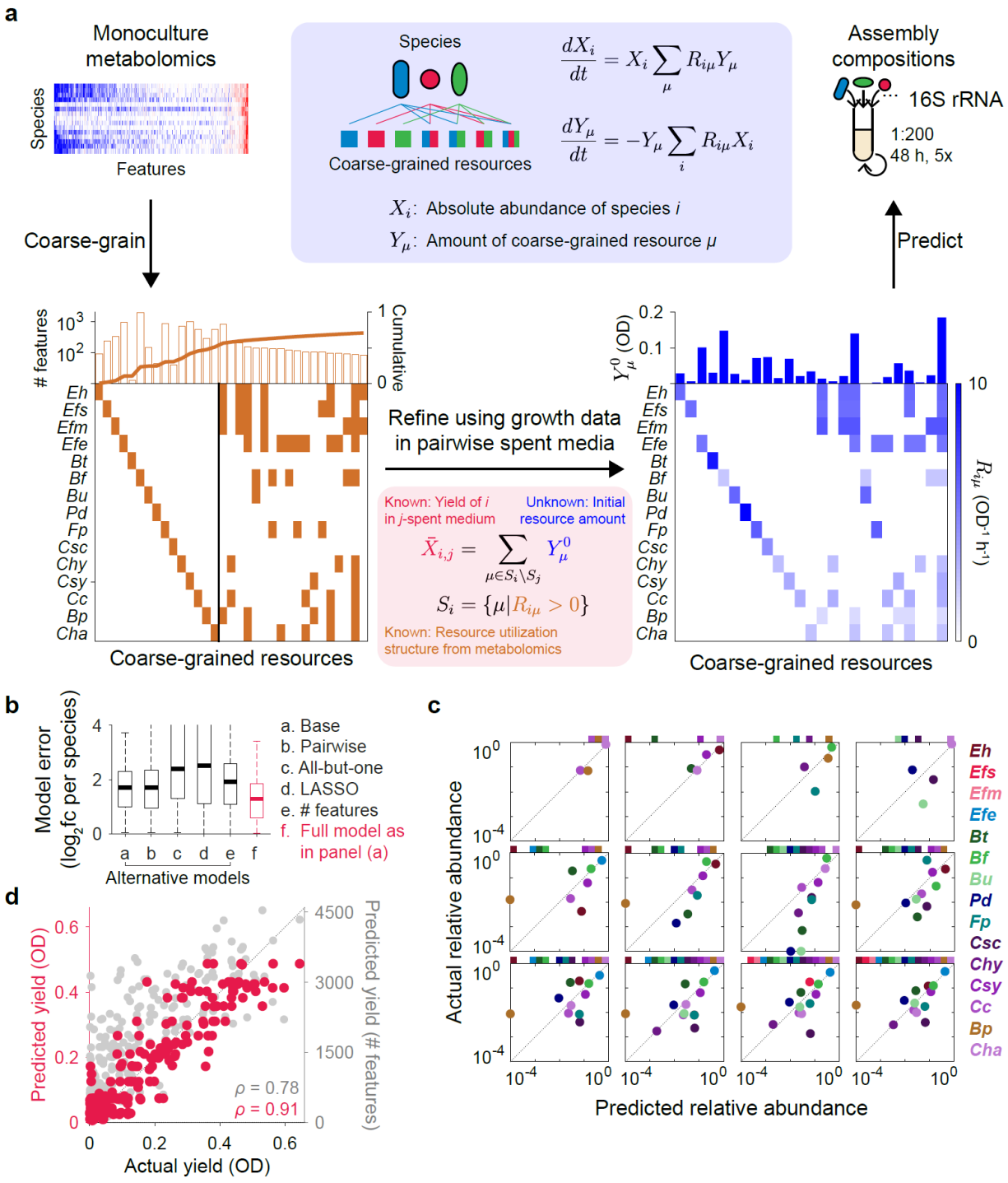

Figure 3: A consumer-resource model based on monoculture metabolomics and growth in spent media predicts community assembly.

a) Schematic for predicting community assembly using a coarse-grained CR model (**Methods**). Metabolomic features were grouped into a coarse-grained resource if they were depleted by the same set of species. The resulting resource utilization

structure (orange, left) was combined with growth data in pairwise spent media to infer resource levels and consumption rates via linear regression (blue, right). Coarse-grained resources with initial amount inferred to be $<10^{-4}$ were removed from the model and not displayed. Shown are the species-specific resources and the 18 coarse-grained resources with the most constituent features, which together accounted for 71% of all features and minimized the AIC for the regression. The resulting CR model was used to predict the composition of 185 random assemblies and compared against experimentally determined relative abundances (**Methods**).

b) The CR model based on metabolomics and pairwise spent-media experiments achieved the lowest mean error out of all models considered. Model error for an assembly was defined as the magnitude of $\log_2$(fold-change) ("fc") between actual and predicted relative abundance averaged across species in the assembly. Shown are box plots denoting the mean error (thick central mark), the 25th and 75th percentiles (box), and the extremes (dashed lines) across all assemblies tested for the best model (red) and alternative models (black), which include 1) models with hypothetical resource utilization structures: the base model consisting of the species-specific resource groups, the base model plus all pairwise niche overlaps, and the base model plus all 15 all-but-one niche overlaps; 2) a regularized regression approach to determine the resource utilization structure; and 3) an approach to approximate resource levels based on feature counts only without using pairwise spent-media experiments (**Methods**). The model in (a) was significantly better than all other models by the Mann-Whitney U-test.

c) Assembly predictions approximately matched experimental data. Each panel shows one assembly. Twelve examples with varying community size were randomly chosen from the 185 combinations tested. Shown are mean relative abundances across replicates. Colored squares along the top of each panel are placed at the same relative location, and indicate species that were present in the inoculum of that assembly. The relative abundances of undetected species were set to 10^{-4} for visualization.

d) Regressed resource levels Y_μ^0 (red) recapitulated yield in pairwise spent media better than feature counts alone (gray) (ρ = 0.91 vs 0.78, respectively).

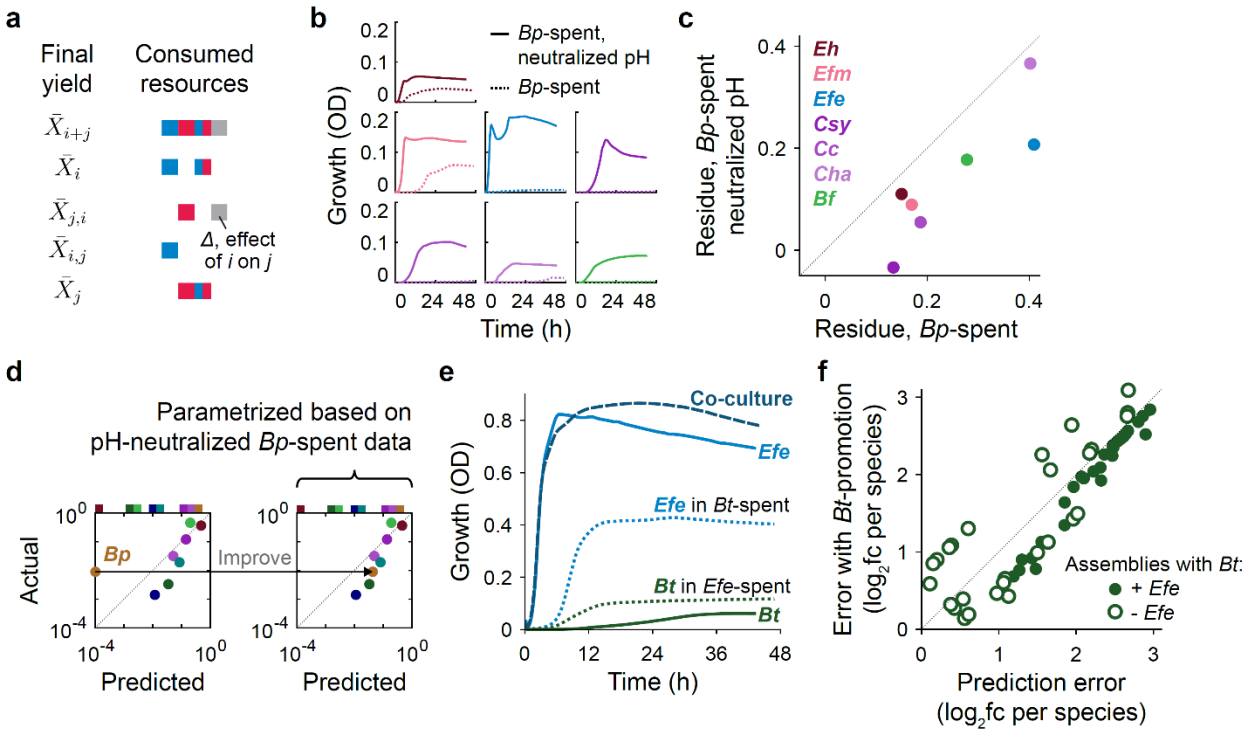

1005

1006 **Figure 4: Strategies for incorporating pH and metabolic cross-feeding interactions**
1007 **into the CR model.**

1008 a) Schematic for interpreting resource competition residues in the presence of
1009 additional contributions to growth from interactions other than resource
1010 competition as described by Eq. 1.

1011 b) pH-mediated interactions involving *Blautia producta* (*Bp*). Shown are growth
1012 curves in *Bp*-spent medium and *Bp*-spent medium with neutralized pH for the
1013 subset of species that grew more quickly than *Bp* in monoculture.

1014 c) Resource competition residues became less positive and closer to zero after
1015 neutralizing the pH of *Bp*-spent medium (**Methods**).

1016 d) Model predictions improved after parametrization based on growth data in pH-
1017 neutralized *Bp*-spent medium. Shown are predictions for an example assembly as
1018 in **Fig. 3c**.

1019 e) *Escherichia fergusonii* (*Efe*) promoted *Bacteroides thetaiotaomicron* (*Bt*) growth.
1020 *Bt* grew more quickly and to higher yield in *Efe*-spent medium, the only case of
1021 growth promotion in spent medium out of all 210 ordered pairs.

1022 f) Errors of model predictions after incorporating the *Efe*-*Bt* interaction into the model.
1023 Shown are prediction errors for the CR model described in **Fig. 3a** and the same

model with a fixed boost to the predicted abundance of *Bt* equal to the difference in yields between *Bt* in *Efe*-spent medium and in monoculture. Shown are all assemblies with *Bt*, including those that also contained *Efe* (filled) and those that did not contain *Efe* (empty). Assemblies with *Efe* were always better predicted when *Bt*-promotion was included, whereas predictions of assemblies without *Efe* were better or worse in an apparently random manner.

EXTENDED DATA FIGURES

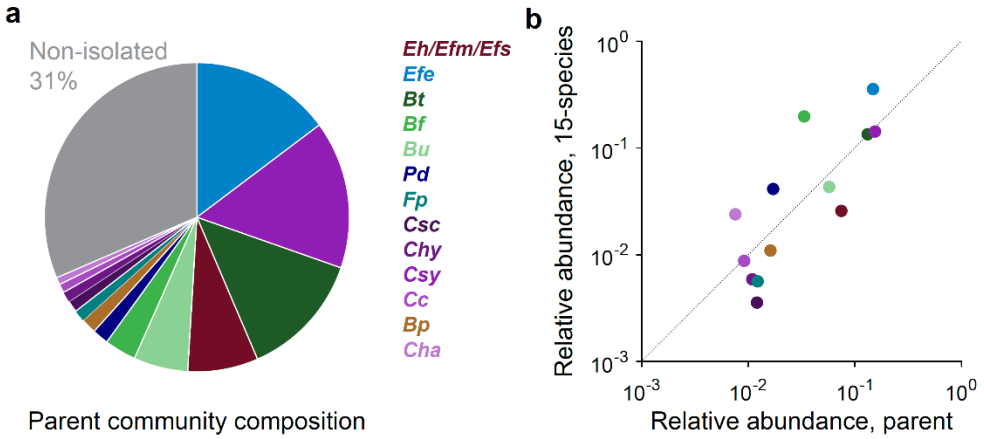

Extended Data Figure 1: The 15 species studied here represent a tractable model system for humanized mice gut microbiota.

a) The 15 isolates were obtained from the same parent community, which was derived by culturing a humanized mice fecal sample. Pie chart shows relative abundance of isolated (colored) and non-isolated (gray) species. The 15 isolates accounted for 69% of the composition of the parent community.

b) The composition of the 15-species assembly was highly correlated with the composition of the parent community (ρ = 0.80).

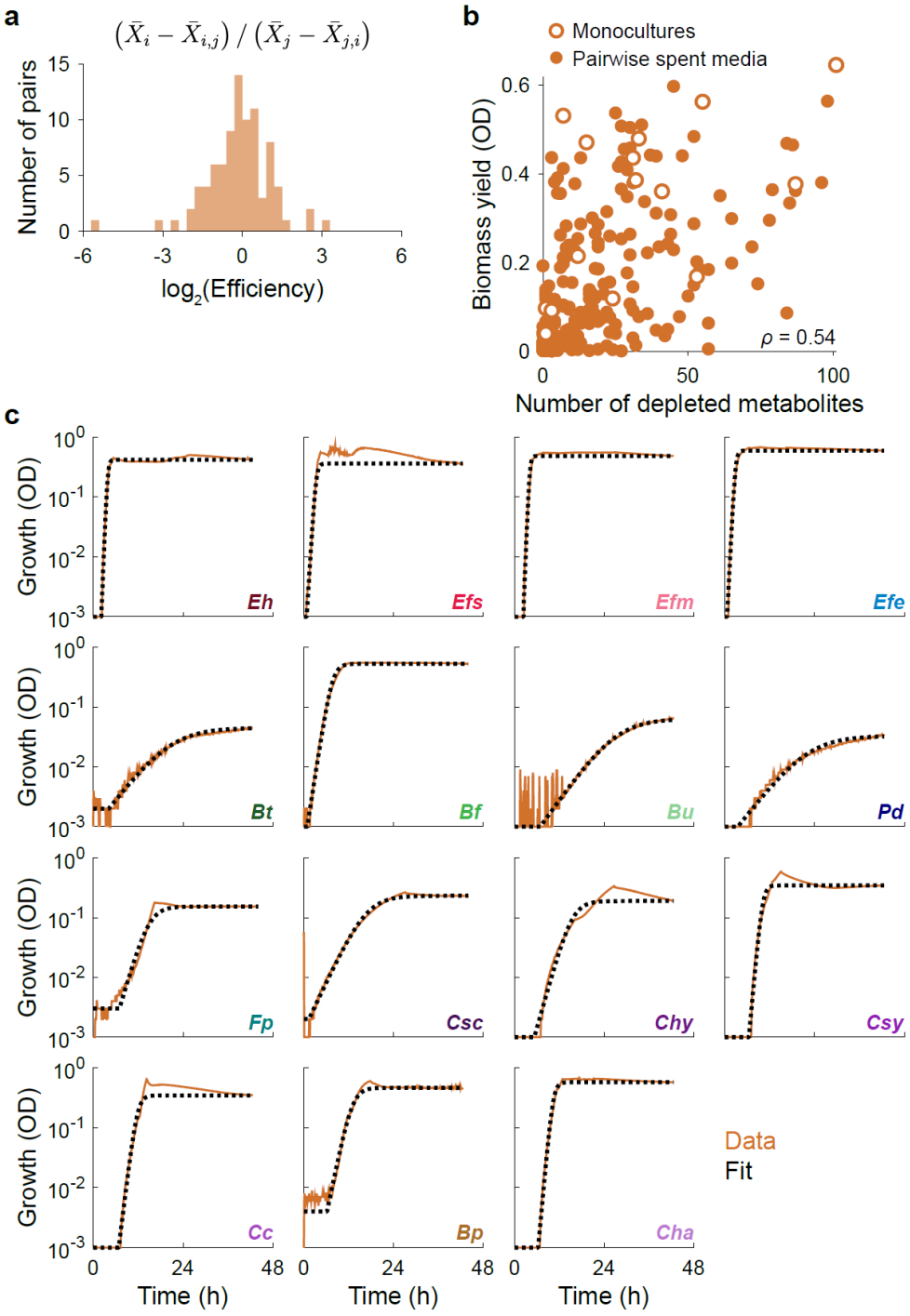

Extended Data Figure 2: Model assumptions.

a) The 15 species converted resources to biomass with similar efficiencies. The efficiency of species i for the conversion of the resource shared with species j was defined as $(\bar{X}_i - \bar{X}_{i,j})/(\bar{X}_j - \bar{X}_{j,i})$. If the efficiency equals one, then Eq. 1 is satisfied. The distribution of $\log_2$(efficiency) across unique ordered pairs was

centered about zero with a narrow width, except for a few outliers for which differences between yields in monoculture and spent medium were small compared to measurement error.

b) The number of annotated features that were depleted was correlated with biomass yield in monocultures and pairwise spent-media experiments, analogous to **Fig. 2c**. The correlation is not as strong as when unannotated features were also included, suggesting that unannotated features are informative for species growth.

c) Monoculture growth curves (orange) were well fit by Eq. 2 for one species and one resource (black; **Methods**).

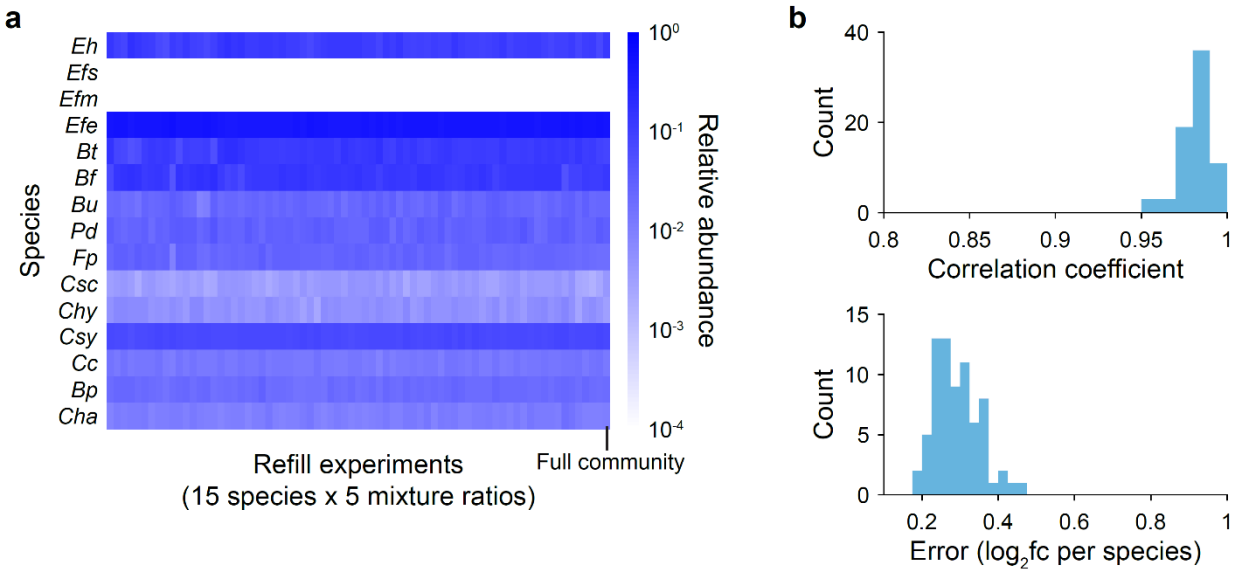

Extended Data Figure 3: Assembly compositions were independent of initial values.

a) Relative abundances at steady state in refill experiments. Each column represents one experiment, in which a dropout assembly with 14 of the 15 species was mixed with a monoculture of the dropped-out species at various ratios (1:1, 1:10, 1:100, 1:1,000, and 1:10,000). All 15 species × 5 ratios were tested, and all are shown except for 3 experiments with idiosyncratic sequencing errors. The compositions were virtually indistinguishable from each other and from the full 15 member community, which is shown in the last column.

b) Histogram of the correlation coefficient (top) and mean absolute error in $\log_2$(fold-change) (bottom) between the relative abundances in each refill experiment and the full 15-species community.

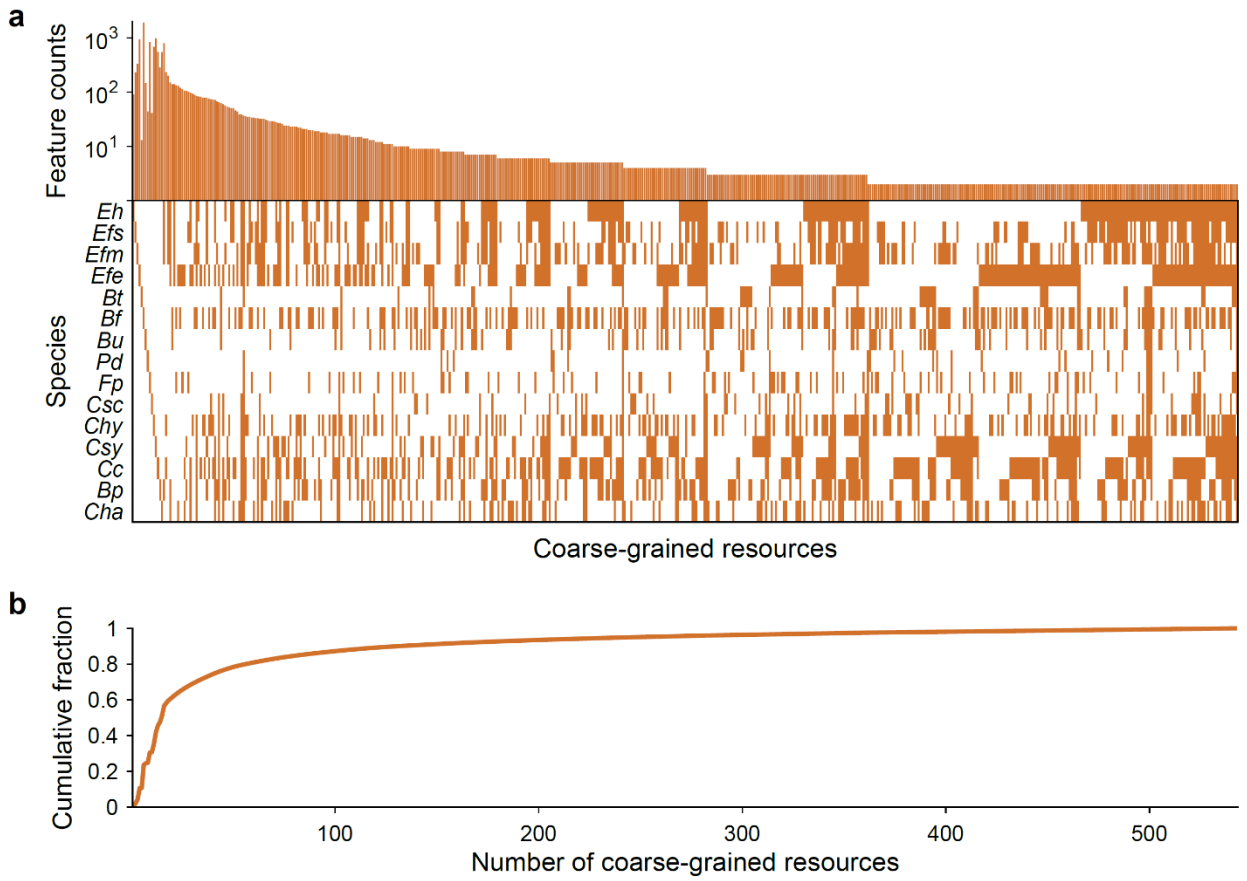

Extended Data Figure 4: Metabolomics-derived coarse-grained resource groups.

a) The structure of metabolomics-derived coarse-grained resource groups. A metabolomic feature was considered depleted if it decreased by >100-fold compared to fresh medium, and features that shared the same set of depleting species were grouped together into a coarse-grained resource group, shown as one column in the matrix. The number of features in each resource group is shown in the bar plot above each column. Only groups with more than one constituent feature are shown.

b) The cumulative fraction of the number of metabolomic features as a function of the number of coarse-grained resource groups included, starting with the leftmost column in (a).

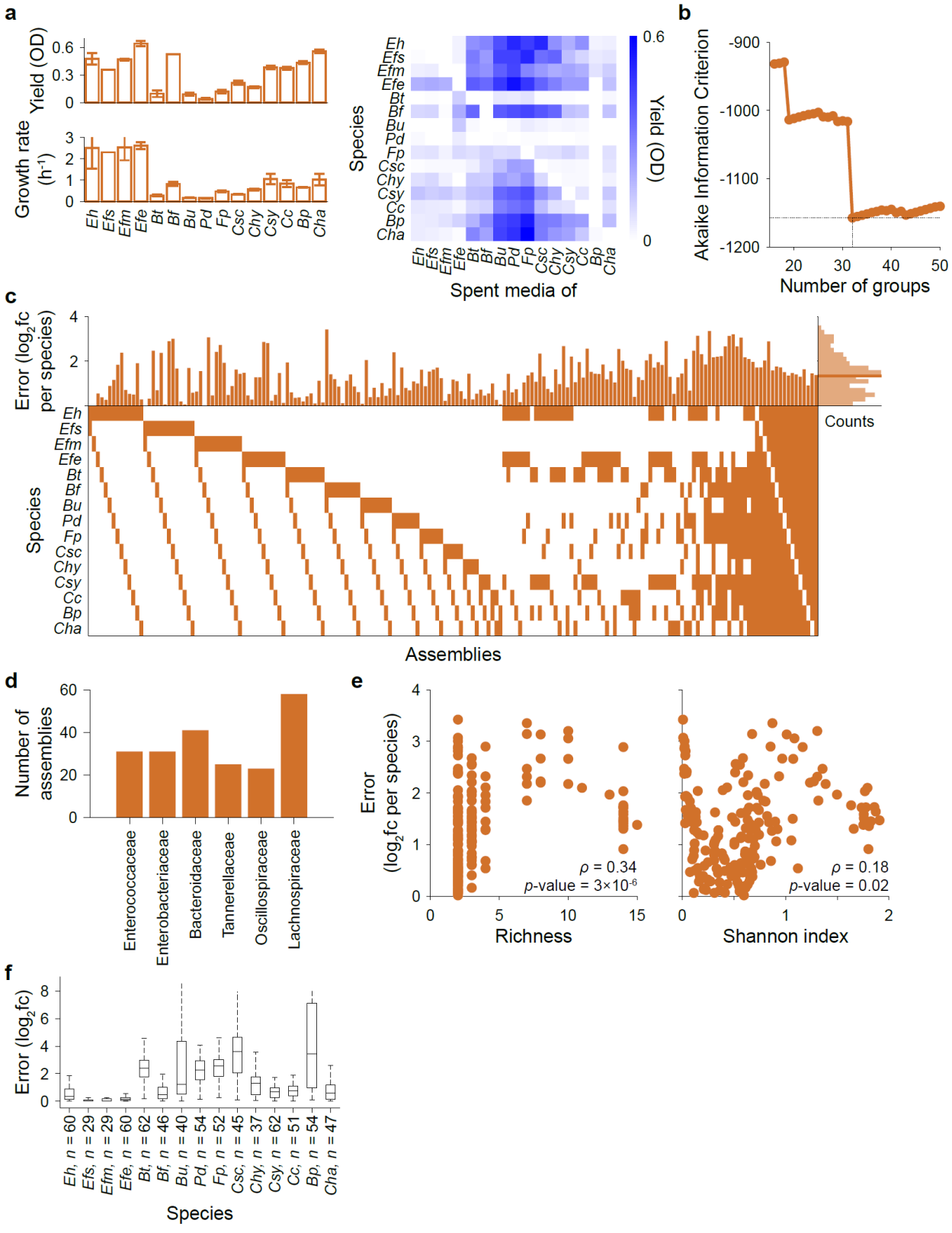

Extended Data Figure 5: Regression input, regression optimization, and prediction errors.

a) Yield and growth rate in monocultures (left) and yield in pairwise spent media (right) were used to refine metabolomics-based resource utilization structures (**Methods**). Shown are mean values across replicates. Error bars denote the standard error of the mean.

b) Determination of resource utilization structure by minimization of the AIC (**Methods**). Minimization was carried out over the top M coarse-grained resource groups with the most constituent features. The AIC-minimizing set of resource groups is shown in **Fig. 3a**.

c) Prediction error for each assembly for the coarse-grained CR model shown in **Fig. 3a**. Shown are all 185 assemblies tested. Errors were calculated using mean relative abundances across replicates. Each column represents one assembly, and the matrix denotes the species that were initially present in each assembly. A histogram of prediction errors and the mean error (solid line) are also shown.

d) The number of assemblies, out of the 64 assemblies containing 3 to 13 species, that contained at least one species from a given family is >30 for every family, indicating that the random combinations tested were taxonomically diverse.

e) Error for each assembly was only weakly correlated with the initial richness (left) or the Shannon index (right) of the community, suggesting that model performance was not dependent on community diversity.

f) Error for each species across all assemblies. The number of assemblies n containing each species is shown. Box plot denotes the median (central mark), 25^{th} and 75^{th} percentiles (box), and extremes (dashed lines).

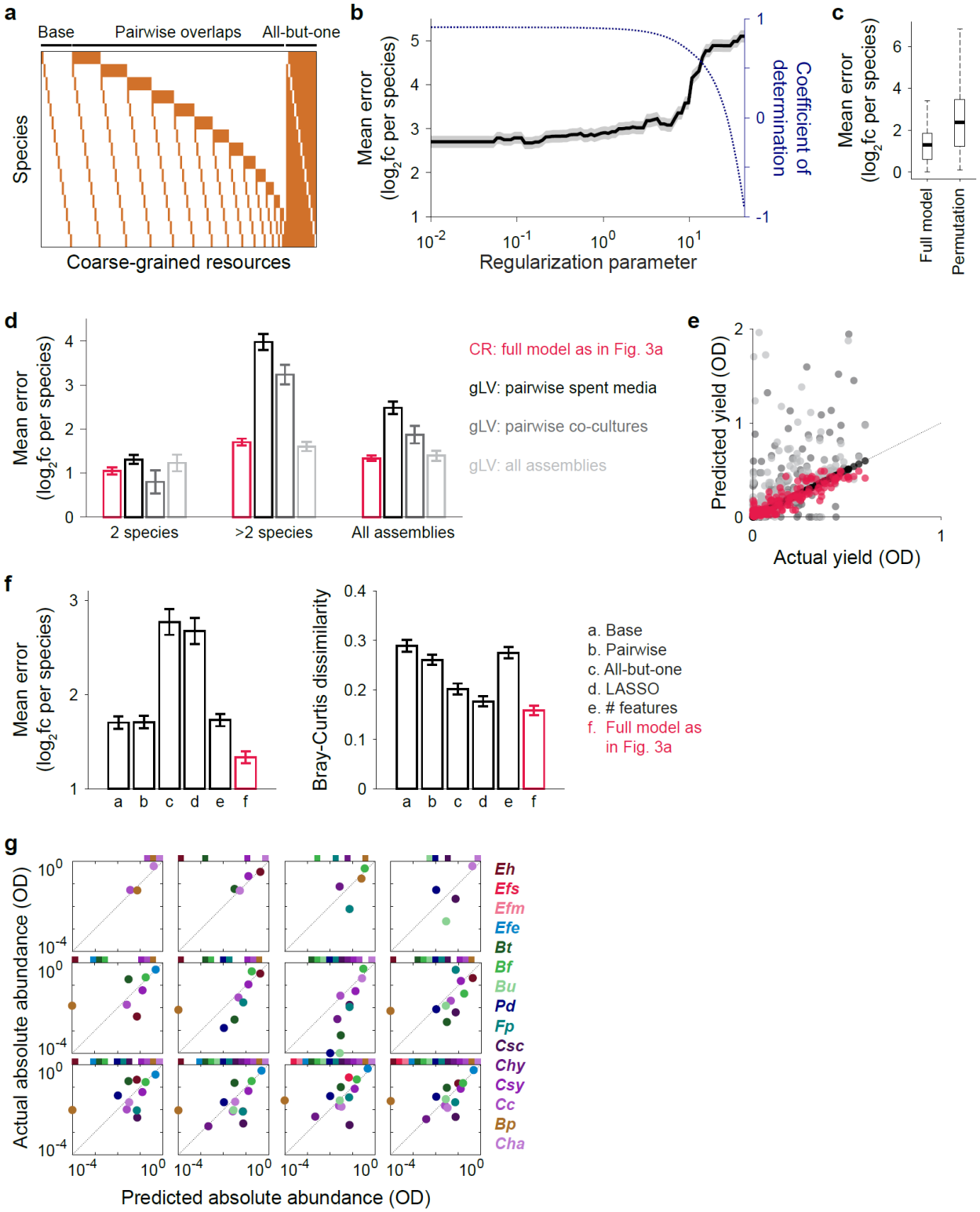

Extended Data Figure 6: Other approaches to predict assembly composition performed worse than the coarse-grained CR model based on metabolomics and pairwise spent-media experiments.

a) Hypothetical resource utilization structures. The “base” structure was defined as the set of species-specific resource groups. On top of the base structure, pairwise niche overlaps consumed by only two species and all-but-one niche overlaps consumed by 14 of the 15 species were also tested. Model performance using these hypothetical structures are shown in **Fig. 3b**.
b) Performance of utilization structures selected by regularized regression on all detected resource groups (**Methods**). Shown are mean errors and coefficients of determination for LASSO fits. Shading denotes standard error of the mean.
c) Prediction error of the full model as in **Fig. 3a** (left) versus model predictions after randomly shuffling species identity (right).
d) The CR model achieved comparable performance as a gLV model fitted to all assembly data. Shown are mean errors of model predictions for co-culture assemblies, assemblies of more than two species, and all assemblies. Error bars denote standard error of the mean. Colors denote different models (**Supplementary Text**): the CR model (orange); and gLV models parametrized using pairwise spent-media experiments (black), species abundances in pairwise co-cultures (dark gray), or species abundances in all assemblies (light gray).
e) gLV models parametrized using assembly data failed to predict yield in pairwise spent-media experiments.
f) The coarse-grained CR model was the best performing model for both the mean absolute error of $\log_2$(fold-change) and the commonly used Bray-Curtis dissimilarity metric, defined as $1 - \sum_{i=1}^{N} \min\left(x_i^{\text{actual}}, x_i^{\text{predicted}}\right)$. Shown are the same models as in **Fig. 3b**.
g) The model successfully predicted absolute abundances, obtained by multiplying relative abundances by culture yield in OD. Panels are representative assemblies, analogous to **Fig. 3c**.

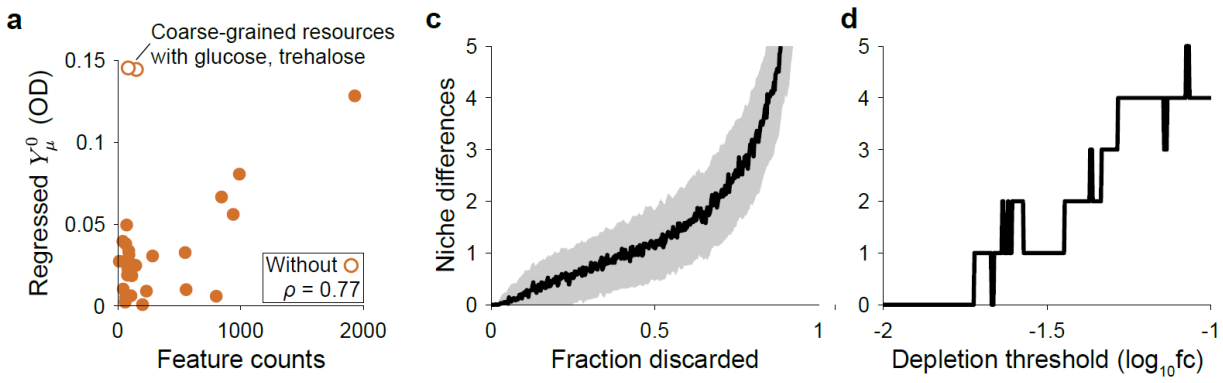

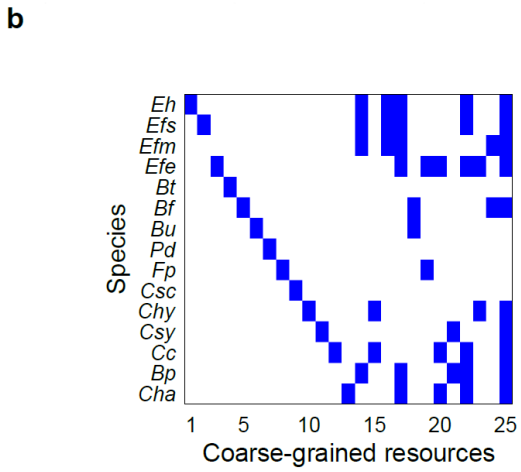

1 Nicotinamide riboside Asn-Arg N-Acetylglucosamine	**2** Ala-Asn Leu-Asp Gln-Thr Phe-Asp Glu-Thr Met-Asp	**3** Carnosine Dihydrobiopterin Pro-Glu Ser-Gln Glutathione Asn-Gln			
4	**5** Tyr-Leu Gln-Ala Val-Phe Phe-Phe His-Tyr Tyr-Phe	**6** Pyridoxamine			
7 Arg-Glu Arg-Met Pro-Lys Ser-Arg Leu-Arg Arg-Ile	**8** Lys-Pro Gly-Asn Pro-Thr Pro-Phe Gly-Pro Leu-Asn	**9** 3'-O-methylinosine Dimethylaminopurine N6-Methyladenine Pterin			
10 Gly-Trp	**11** Lys-Leu Lys-Ile Ethanolamine Lys-Ile-Arg Lys-Lys Lys-Val-Lys	**12**	**13**	**14** PyroGlu-Val PyroGlu-Met PyroGlu-Trp	**15** His-Met Ile-Ile Ile-Val Thr-Gly Val-His Ile-Gln
16	**17** Trehalose	**18**	**19** cAMP cGMP	**20** Hypoxanthine Xanthine	**21** Histidine Glu-Gln
22 Cytidine 5-Methylcytidine Uridine 2-Deoxyuridine	**23** Tyr-Gly Thr-Asp Val-Asp Ala-Asp Pro-Thr	**24**	**25** Glucose		

Extended Data Figure 7: Biological basis and robustness of the metabolomics-based resource competition landscape.

a) Regressed resource levels were correlated with feature counts across coarse-grained resources. Two outliers (empty symbols) contained features identified as the simple sugars glucose and trehalose. Without these two outliers, correlations

were high (ρ = 0.77), indicating that the regression refined metabolomics-based estimations.

b) Annotated metabolomic features suggest that diverse peptide utilization capabilities shape the resource competition landscape. Examples of annotated metabolomic features within each coarse-grained resource group for the CR model shown in **Fig. 3a**. Resource groups with empty fields did not have any annotated features.

c) Coarse-graining is robust to uncertainty in peak calling and quantitation. “Niche differences” denote the number of groups within the top 50 resource groups with the most constituent features that are different from the set used in the original analysis (**Extended Data Fig. 4**). Uncertainty in peak calling was simulated by discarding a random fraction of features. Up to half of the features could be discarded without affecting the identity of the resource groups with the most constituent features. Shading denotes the standard deviation of niche differences across random instances of feature removal.

d) Uncertainty in quantitation was simulated by varying the threshold fold-change for classifying depletion. The depletion threshold could be varied over an order of magnitude without changing more than 5 of the 50 largest groups.

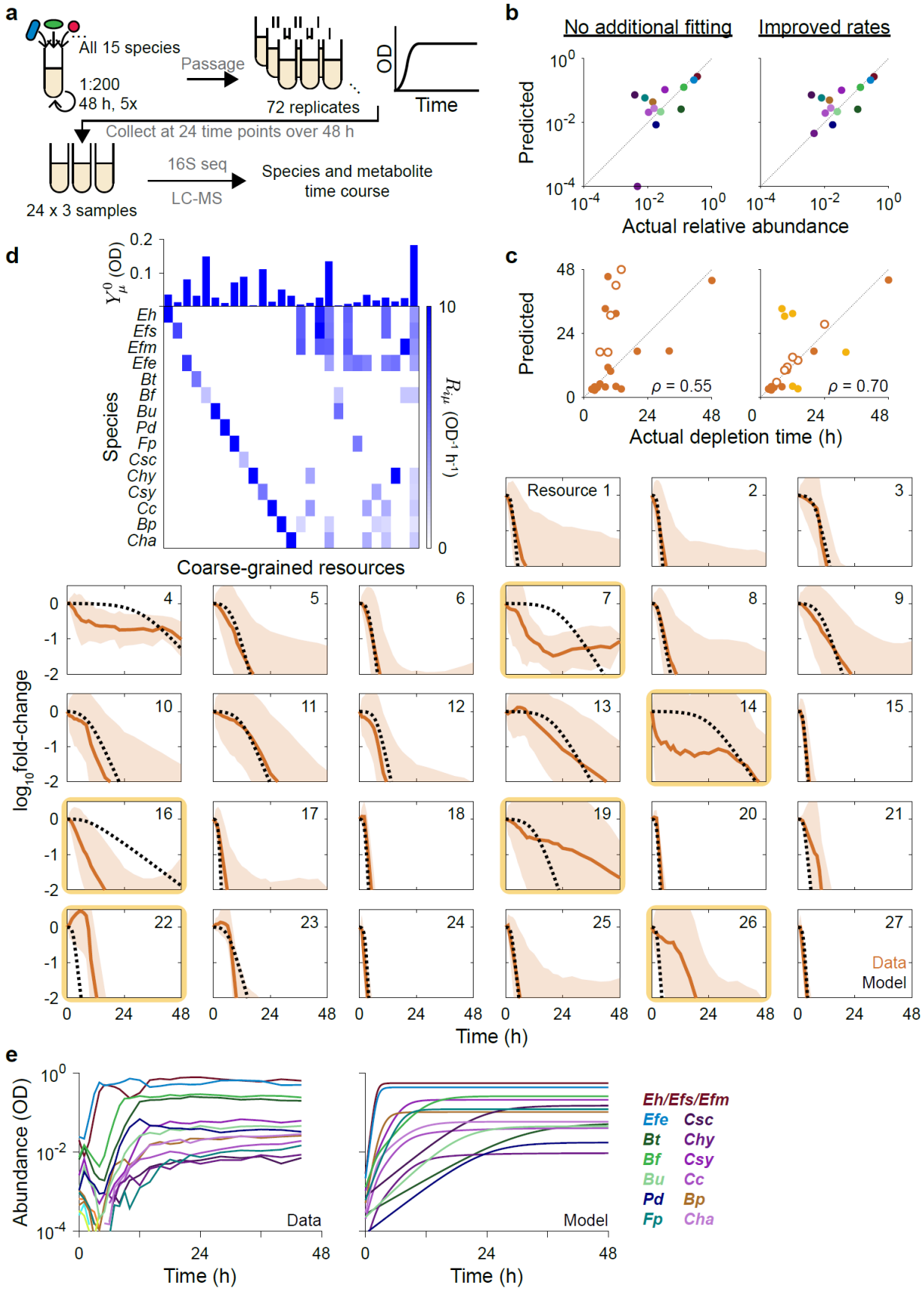
a
All 15 species
1:200
48 h, 5x
Passage
72 replicates
OD
Time
Collect at 24 time points over 48 h
24 x 3 samples
16S seq
LC-MS
Species and metabolite time course
b
No additional fitting
Improved rates
Predicted
Actual relative abundance
c
Predicted
ρ = 0.55
ρ = 0.70
Actual depletion time (h)
d
Species
Eh
Efs
Efm
Efe
Bt
Bf
Bu
Pd
Fp
Csc
Chy
Csy
Cc
Bp
Cha
Coarse-grained resources
Resource 1
log10 fold-change
Data
Model
Time (h)
e
Abundance (OD)
Data
Model
Time (h)
Eh/Efs/Efm
Efe
Csc
Bt
Chy
Bf
Csy
Bu
Cc
Pd
Bp
Fp
Cha

Extended Data Figure 8: The CR model captured metabolite depletion dynamics at a coarse-grained level.

a) Experiment schematic. The full 15-species community was assembled and passaged to reach ecological steady state. Replicate cultures were inoculated from the steady-state culture, and 3 replicates were collected at 24 time points throughout the next growth cycle. Sequencing and metabolomics data were obtained for all samples (**Methods**).

b) The CR model predicted assembly compositions. The parametrization based on pH-neutralized *Bp*-spent medium experiments was used (**Fig. 4**). One species (*C. hylemonae*) was incorrectly predicted to be undetectable, which could be remedied by using metabolite depletion rates to improve the model as in (c).

c) The CR model captured the depletion time of coarse-grained resources, defined as when the $\log_{10}$(fold-change) first decreases below -1. Without any modification, the model achieved a reasonable performance (ρ = 0.55, left). Several outliers were species-specific resource groups (empty symbols). The model was improved by adjusting the consumption rates of these outlier groups to match their depletion times (ρ = 0.71, right), which simultaneously improved predictions for species abundances as in (b). The remaining outliers are highlighted in yellow.

d) Resource dynamics were captured at a coarse-grained level. Each panel shows the dynamics of a coarse-grained resource. The matrix shows the set of coarse-grained resources included in the model. (Parametrization using pH-neutralized *Bp*-spent medium experiments led to the incorporation of 2 additional resource groups with non-zero Y_μ^0 compared to the parametrization shown in **Fig. 3a**.) Solid lines show the mean $\log_{10}$(fold-change) across all metabolomic features in a group. Shading shows the standard deviation. Dotted lines show the predictions of the improved model. Outlier groups in (c) are highlighted.

e) The model also captured species abundances over time in the full community.

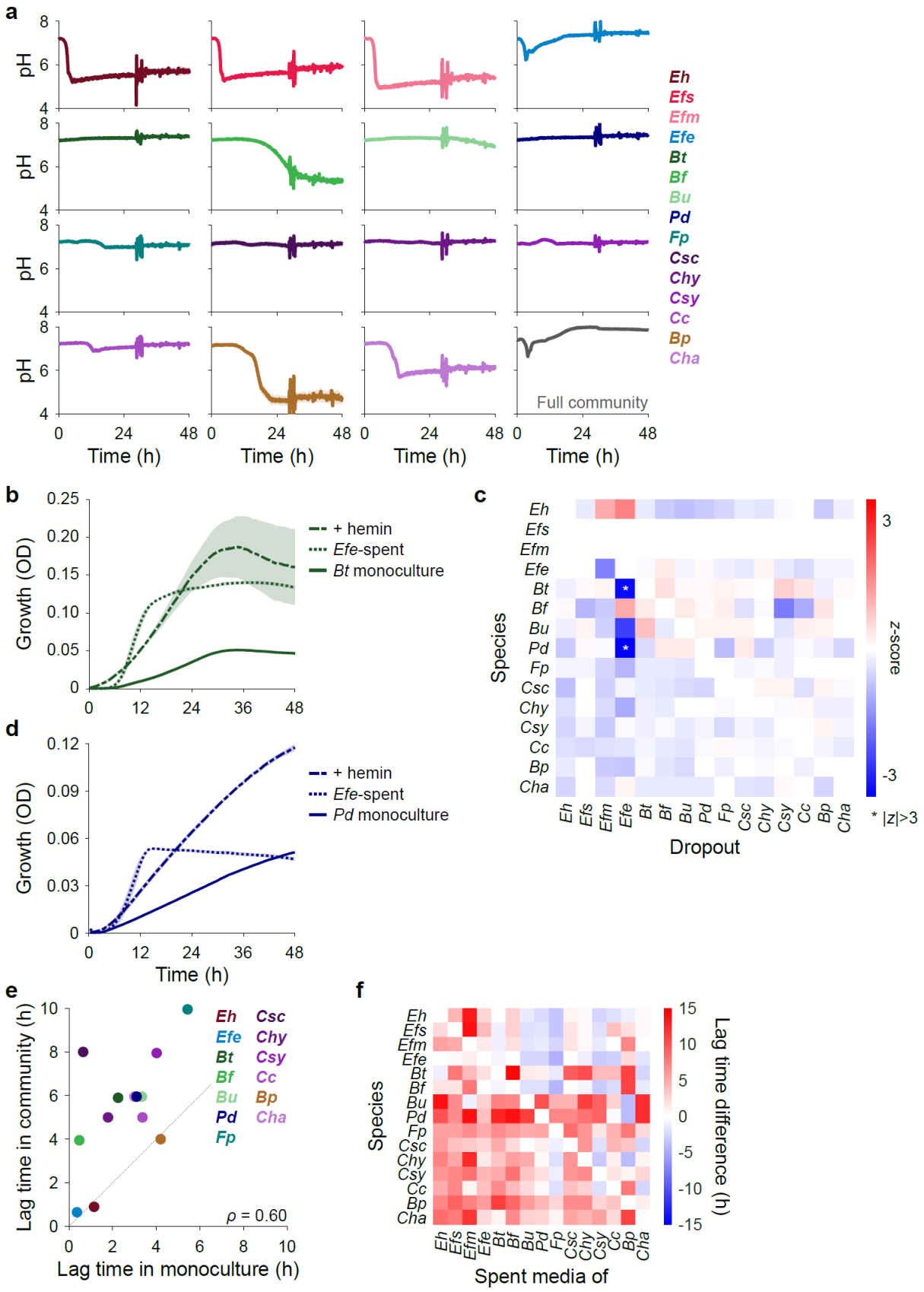
a
pH
Time (h)
Full community
Eh
Efs
Efm
Efe
Bt
Bf
Bu
Pd
Fp
Csc
Chy
Csy
Cc
Bp
Cha
b
Growth (OD)
+ hemin
Efe-spent
Bt monoculture
c
Species
Dropout
z-score
* |z|>3
d
Growth (OD)
+ hemin
Efe-spent
Pd monoculture
Time (h)
e
Lag time in community (h)
Lag time in monoculture (h)
ρ = 0.60
f
Species
Spent media of
Lag time difference (h)

Extended Data Figure 9: The model can be extended to incorporate pH, cross-feeding, and lag times.

a) The full community and most species, except for *Blautia producta* and a few other species, did not modify the pH. pH was obtained during growth measurements using BCECF for each species in monoculture and the full 15-species community (**Methods**). Shading denotes standard error of the mean.

b) Growth curves for *Bt* grown in fresh medium (solid line), in *Efe*-spent medium (dotted line), and in fresh BHI plus hemin (dash dotted line). Shown is the mean over replicates. Shading denotes standard error of the mean.

c) Interactions persisted in a community context, and strong interactions in dropout assemblies were rare. Relative abundances in dropout assemblies are shown in terms of *z*-scores. Each column represents a dropout assembly of 14 of the 15 species, with the denoted species left out of the community. Each row represents the *z*-scores of the denoted species, defined as $z_{ij} \coloneqq \left(x_{ij} - \mu_i\right)/\sigma_i$, where x_{ij} is the $\log_{10}$(relative abundance) of species i in the dropout assembly in which species j was left out, and μ_i and σ_i are the mean and standard deviation, respectively, of the $\log_{10}$(relative abundance) of species i across all dropout assemblies. Asterisks denote *z*-scores with absolute value >3.

d) Same as (b) but for *Pd*.

e) Lag times in monoculture and in the full 15-species community were correlated. For the full community, absolute abundances over time were obtained by multiplying relative abundances by culture OD over the time course of the full community. Lag times were extracted by fitting as for monocultures.

f) The difference between the lag time of a species grown in the spent medium of another species and grown in fresh medium was typically positive.

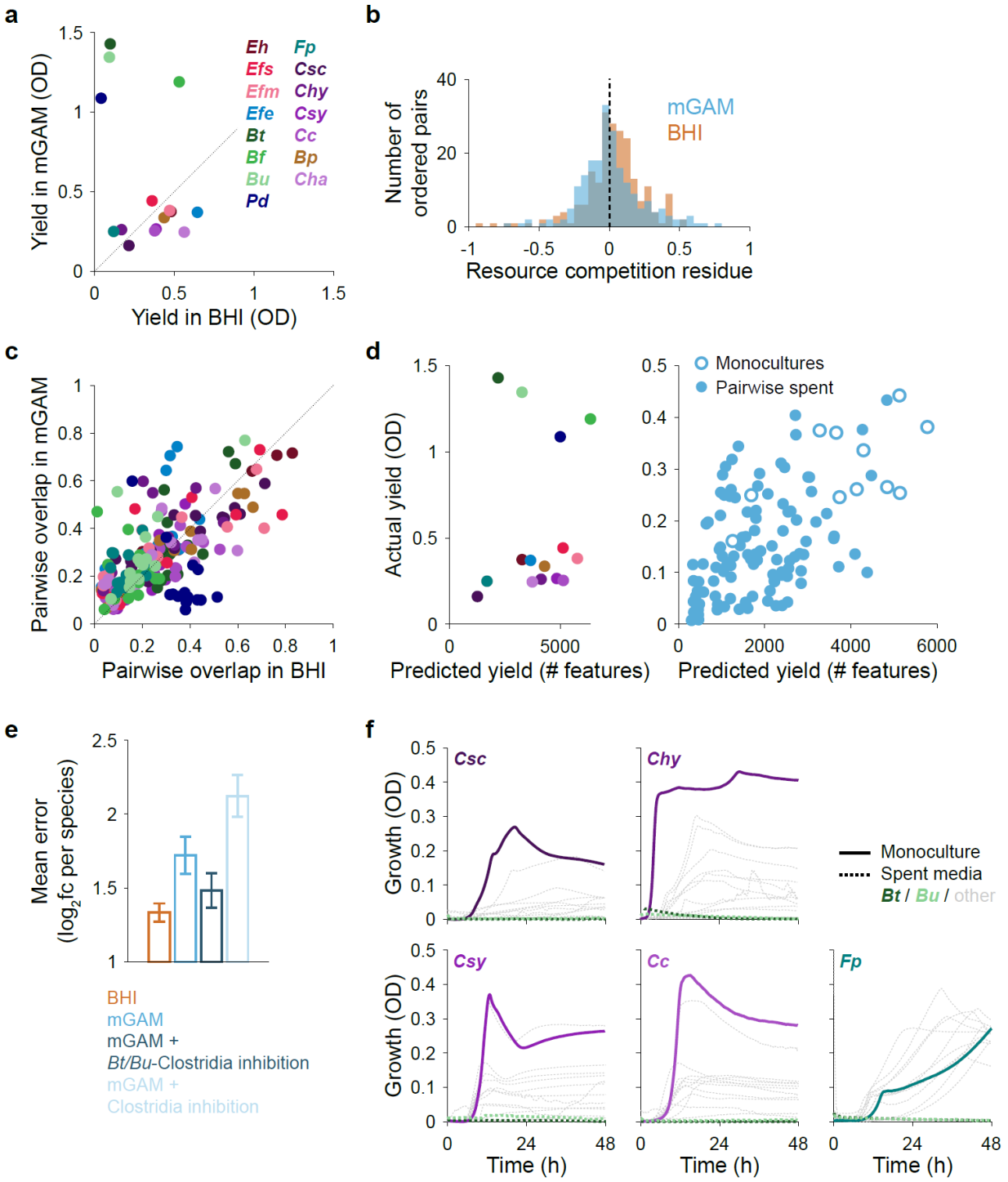

Extended Data Figure 10: Modeling framework was able to predict assembly compositions and interrogate interactions in the complex medium mGAM.

a) Monoculture yields in mGAM differed from those in BHI, particularly for the Bacteroidetes, which exhibited substantially larger yields in mGAM. Shown are mean values across replicates.
b) The distribution of resource competition residues in mGAM was centered about zero, as in BHI (**Fig. 1d**).
c) Pairwise overlaps in metabolomic profiles in mGAM and BHI were correlated (ρ = 0.66). The pairwise overlap between the ordered species pair (i, j) was defined as the number of metabolomic features depleted by both species divided by the number depleted by species i. Shown are all 210 ordered pairs, colored according to species i.
d) Yield in monoculture (left) and pairwise spent-media experiments (right) was correlated with feature counts for experiments not involving the four Bacteroidetes (ρ = 0.54). Pairwise spent-media experiments involving the four Bacteroidetes are not shown.
e) Incorporation of additional interactions significantly and specifically improved model performance in mGAM. Shown are mean errors for model predictions in BHI (orange) and mGAM (blue), parametrized using metabolomics and spent-media experiments in the corresponding media, as well as mean errors for the CR model in mGAM modified to incorporate *Bt*/*Bu*-Clostridia interactions (dark blue) or with ubiquitous Clostridia inhibition (light blue). Error bars denote the standard error of the mean.
f) The 5 Clostridia species exhibited no detectable growth in *Bt*- or *Bu*-spent media. Each panel shows the growth curve of a species in monoculture (solid line) and in pairwise spent media (dotted lines). The color of the solid line denotes the species grown in each panel. The color of the dotted lines denotes the species that generated the spent media. Gray dotted lines show growth curves in all other spent media.